CANCER

Therapeutic strategies for diffuse midline glioma from high-throughput combination drug screening

Grant L. Lin[1], Kelli M. Wilson[2], Michele Ceribelli[2], Benjamin Z. Stanton[3], Pamelyn J. Woo[1], Sara Kreimer[1], Elizabeth Y. Qin[1], Xiaohu Zhang[2], James Lennon[1], Surya Nagaraja[1], Patrick J. Morris[2], Michael Quezada[1], Shawn M. Gillespie[1], Damien Y. Duveau[2], Aleksandra M. Michalowski[4], Paul Shinn[2], Rajarshi Guha[2], Marc Ferrer[2], Carleen Klumpp-Thomas[2], Sam Michael[2], Crystal McKnight[2], Paras Minhas[1], Zina Itkin[2], Eric H. Raabe[5], Lu Chen[2], Reem Ghanem[1], Anna C. Geraghty[1], Lijun Ni[1], Katrin I. Andreasson[1], Nicholas A. Vitanza[1], Katherine E. Warren[6]*†, Craig J. Thomas[2,7]†, Michelle Monje[1,8,9,10,11,12]†

Diffuse midline gliomas (DMGs) are universally lethal malignancies occurring chiefly during childhood and involving midline structures of the central nervous system, including thalamus, pons, and spinal cord. These molecularly related cancers are characterized by high prevalence of the histone H3K27M mutation. In search of effective therapeutic options, we examined multiple DMG cultures in sequential quantitative high-throughput screens (HTS) of 2706 approved and investigational drugs. This effort generated 19,936 single-agent dose responses that inspired a series of HTS-enabled drug combination assessments encompassing 9195 drug-drug examinations. Top combinations were validated across patient-derived cell cultures representing the major DMG genotypes. In vivo testing in patient-derived xenograft models validated the combination of the multi–histone deacetylase (HDAC) inhibitor panobinostat and the proteasome inhibitor marizomib as a promising therapeutic approach. Transcriptional and metabolomic surveys revealed substantial alterations to key metabolic processes and the cellular unfolded protein response after treatment with panobinostat and marizomib. Mitigation of drug-induced cytotoxicity and basal mitochondrial respiration with exogenous application of nicotinamide mononucleotide (NMN) or exacerbation of these phenotypes when blocking nicotinamide adenine dinucleotide (NAD^+) production via nicotinamide phosphoribosyltransferase (NAMPT) inhibition demonstrated that metabolic catastrophe drives the combination-induced cytotoxicity. This study provides a comprehensive single-agent and combinatorial drug screen for DMG and identifies concomitant HDAC and proteasome inhibition as a promising therapeutic strategy that underscores underrecognized metabolic vulnerabilities in DMG.

INTRODUCTION

Diffuse midline gliomas (DMGs) such as diffuse intrinsic pontine glioma (DIPG) are universally lethal central nervous system (CNS) tumors that occur chiefly during childhood (*1*). Despite decades of clinical trials, treatment is limited to radiotherapy. Even with radiotherapy, median overall survival for children with DIPG is only 9 to 11 months (*2*, *3*). Over the past decade, the molecular characterization of DIPG has advanced our understanding of the genetic and epigenetic underpinnings of these tumors, including the identification of a recurrent H3K27M mutation in H3.3 (*H3F3A*) or H3.1 (*HIST1H3B*) histones (*4*, *5*). Mechanistically, the H3K27M mutation results in dysfunction of the Polycomb repressive complex 2 (PRC2) and consequent loss of H3K27 trimethylation, broad epigenetic dysregulation, and oncogenic gene expression. DIPG has recently been reclassified into a broader category of midline gliomas that share the signature H3K27M mutation, including thalamic and spinal cord gliomas (*6*, *7*).

We previously reported a limited chemical screen against a panel of 83 agents in patient-derived DIPG cultures (*8*). That study identified the multi–histone deacetylase (HDAC) inhibitor panobinostat as a promising clinical agent, exhibiting a disease-specific mechanism of restoring H3K27 methylation and normalizing oncogenic gene expression. Those results led to ongoing phase 1 clinical trials of panobinostat in DIPG (NCT02717455, NCT03566199, and NCT03632317) (*9*). Nevertheless, in preclinical DIPG models, resistance to panobinostat emerges, highlighting the need for combinatorial therapeutic strategies (*8*, *10*). Driven by the mechanistic implications of the H3K27M mutation, substantial effort has focused on epigenetic targets, including inhibitors of EZH2, CDK7, and BET family proteins (*10*–*13*). However, a full appreciation of the druggable landscape in DIPG and other DMGs remains lacking.

The application of combinatorial drug therapy has revolutionized prognoses for other cancers such as childhood leukemia (*14*). The development of chemogenomic compound libraries has enabled

[1]Department of Neurology, Stanford University School of Medicine, Stanford, CA 94305, USA. [2]Division of Preclinical Innovation, National Center for Advancing Translational Sciences, National Institutes of Health, Rockville, MD 20850, USA. [3]Center for Childhood Cancer and Blood Diseases, Abigail Wexner Research Institute at Nationwide Children's Hospital, The Ohio State University College of Medicine, Columbus, OH 43205, USA. [4]Laboratory of Cancer Biology, National Cancer Institute, National Institutes of Health, Bethesda, MD 20892, USA. [5]Department of Pathology, Johns Hopkins University School of Medicine, Baltimore, MD 21287, USA. [6]Pediatric Oncology Branch, National Cancer Institute, National Institutes of Health, Bethesda, MD 20892, USA. [7]Lymphoid Malignancies Branch, National Cancer Institute, National Institutes of Health, Bethesda, MD 20892, USA. [8]Department of Neurosurgery, Stanford University School of Medicine, Stanford, CA 94305, USA. [9]Department of Pediatrics, Stanford University School of Medicine, Stanford, CA 94305, USA. [10]Department of Pathology, Stanford University School of Medicine, Stanford, CA 94305, USA. [11]Stanford Cancer Institute, Stanford University School of Medicine, Stanford, CA 94305, USA. [12]Stanford Institute for Stem Cell and Regenerative Medicine, Stanford University School of Medicine, Stanford, CA 94305, USA.
*Present address: Pediatric Oncology, Dana-Farber Cancer Institute/Boston Children's Hospital, Boston, MA 02115, USA.
†Corresponding author. Email: katherinee_warren@dfci.harvard.edu (K.E.W.); craigt@mail.nih.gov (C.J.T.); mmonje@stanford.edu (M.M.)

target-based drug discovery and, used in a combination matrix approach, allows exploration of thousands of drug-drug pairs for potential synergy (*15*–*17*).

We sought to comprehensively characterize the druggable cell-intrinsic vulnerabilities in DIPG and other DMGs and identify promising therapeutic agents. High-throughput drug screening using two mechanistically annotated collections of approved and investigational drugs in six well-characterized patient-derived DIPG cell cultures resulted in a dataset of 19,936 single-agent dose responses. On the basis of this dataset, we performed several combinatorial screens encompassing 9195 distinct drug-drug combinations to identify potential synergies. These single-agent and combination drug responses were used to map the drug and drug-to-drug interaction landscape of the most promising agents based on potency, mechanistic class enrichment, and predicted blood-brain barrier penetrance. Promising drugs and drug combinations were evaluated in vitro across an expanded panel of representative patient-derived DMG cell cultures and in vivo within orthotopic xenograft models. These studies identified panobinostat and marizomib as a promising drug combination. Investigations of molecular mechanisms that drive the cytotoxic synergy of this drug combination revealed that DIPG and other DMGs are metabolically vulnerable.

RESULTS

Comprehensive high-throughput drug screening demonstrates classes of mechanistic vulnerabilities of DIPG

We performed multiple single-agent screens in a total of six DIPG cell culture models (JHH-DIPG-1, SU-DIPG-IV, SU-DIPG-VI, SU-DIPG-XIII, SU-DIPG-XVII, and SU-DIPG-XXV) using our internal mechanism interrogation plate (MIPE) 4.0 and 5.0 libraries. All data are publicly available and searchable via the PubChem database (https://pubchem.ncbi.nlm.nih.gov/) (BioAssay Identifier AID: table S1 in data file S1) and at https://matrix.ncats.nih.gov/. These libraries contain a total of 2706 unique agents (257 unique to MIPE 4.0, 764 unique to MIPE 5.0, and 1685 conserved in both libraries) (Fig. 1A, fig. S1A, and table S2 in data file S1) (*16*). These libraries include multiple inhibitors for well-explored oncogenic targets [for instance, phosphoinositide 3-kinase (PI3K) and heat shock protein 90 (HSP90)] while simultaneously encompassing mechanistic diversity, targeting more than 860 distinct mechanisms of action (MoAs; table S3 in data file S1). Together, these screens generated 19,936 dose-response signatures. Analysis of the MIPE 5.0 outcomes highlighted similar drug sensitivity profiles among the screened cell cultures, generating a coherent database of DIPG chemical vulnerabilities used to prioritize compounds for further analyses (fig. S1, B and C). We used *Z*-transformed area under the curve (*Z*-AUC) to distinguish inactive and active drug responses. Agents with *Z*-AUC values less than −0.85 in at least three of the cell cultures in the MIPE 5.0 dataset were classified as "hits," identifying 371 hits. Several MoAs relevant to DIPG pathogenesis were enriched among these agents, including HDAC, proteasome, insulin-like growth factor receptor (IGFR), mitogen-activated protein kinase kinase (MEK), and PI3K inhibitors (Fig. 1B and table S4 in data file S1). Dose-response curves for representative agents of these MoAs are shown in Fig. 1C. Agents from these mechanistic classes demonstrated a relatively wide potency range, with proteasome inhibitors being, on average, the most potent drug class (Fig. 1D and fig. S1D). Several hits outperformed agents in currently active or recently completed DIPG clinical trials (Fig. 1, A and E, Table 1, and table S5 in data file S1), and some agents currently in clinical studies for DIPG failed to elicit a meaningful cytotoxic response (see Table 1 for examples). Cautious interpretation of these data is advocated because several trials (examples are detailed in Table 1) examine combinations of these drugs and/or the coadministration of radiation therapy. Our screens also examined drug classes of current preclinical interest in DIPG. Bromodomain inhibitors, for example, are of emerging interest in DMG and glioblastoma (*12*). Of the 15 bromodomain inhibitors included in our MIPE 5.0 screens, only two (ARV-771 and mivebresib) demonstrated activity beyond our *Z*-AUC cutoff.

Because the ability of these candidates to penetrate the blood-brain barrier is crucial for their development as systemically delivered DMG therapies, we incorporated CNS penetration as a metric to judge the translational potential of drugs from our screens. To that end, we applied the CNS multiparameter optimization desirability (MPO) scoring system to all agents in the MIPE 5.0 library (*18*). Reassessing the potential of hits while considering their MPO scores (increasing MPO value indicates more likely CNS exposure) provided additional information (Fig. 1F). Akin to the cytotoxicity outcomes, there was a range of MPO scores for key drug classes and agents in current clinical evaluation in DIPG (Fig. 1G). Twenty-two agents had strong activity (average *Z*-AUC < −2.0) and predicted CNS exposure (MPO score > 4.4), including several with proven CNS exposure (Table 2 and table S6 in data file S1). Among these was the next-generation proteasome inhibitor marizomib (salinosporamide A), which had strong DIPG cell cytotoxicity [AC_{50} (half maximal activity concentration) < 40 nM in all cell cultures] and validated CNS exposure in humans (Fig. 1H) (*19*, *20*).

Quantitative high-throughput drug-drug combination screening identifies potential combinatory approaches for DIPG

We next evaluated the actions of key drugs of interest from the single-agent screens in high-throughput screen (HTS)–enabled combination assessments (*16*). Both the HDAC inhibitor panobinostat and the proteasome inhibitor marizomib were evaluated versus the entire MIPE 5.0 library, and a third combination experiment was conducted evaluating 45 selected agents in an all-versus-all experiment exploring 990 drug-drug pairs. Additional combination experiments were performed amassing 9195 discrete drug-drug combinations (https://matrix.ncats.nih.gov/).

The examination of panobinostat or marizomib versus the entire MIPE 5.0 library provided insight into the system effect associated with HDAC and proteasome inhibitors (Fig. 2A). Panobinostat had broad synergistic interactions with several drug classes, including proteasome inhibitors and signaling modulators including PI3K, IGFR, and MEK inhibitors (Fig. 2, B and C, and table S7 in data file S1). Marizomib displayed a more restricted combination profile, with synergistic cytotoxicity primarily when combined with HDAC inhibitors and, to a lesser extent, HSP90 inhibitors (Fig. 2B and table S8 in data file S1). The MIPE 5.0 library contains 35 different HDAC inhibitors with distinct selectivity profiles across individual HDAC isoforms. Examining each agent's combination profile with marizomib highlighted that pan-HDAC inhibitors (for instance, panobinostat and romidepsin) targeting class I HDACs (HDAC1, HDAC2, and HDAC3) and class II HDACs yielded the highest degree of synergy (Fig. 2D and table S8). HDAC inhibitors that do not target class I HDACs (for instance, TMP-195 and PCI-34051) did not synergize

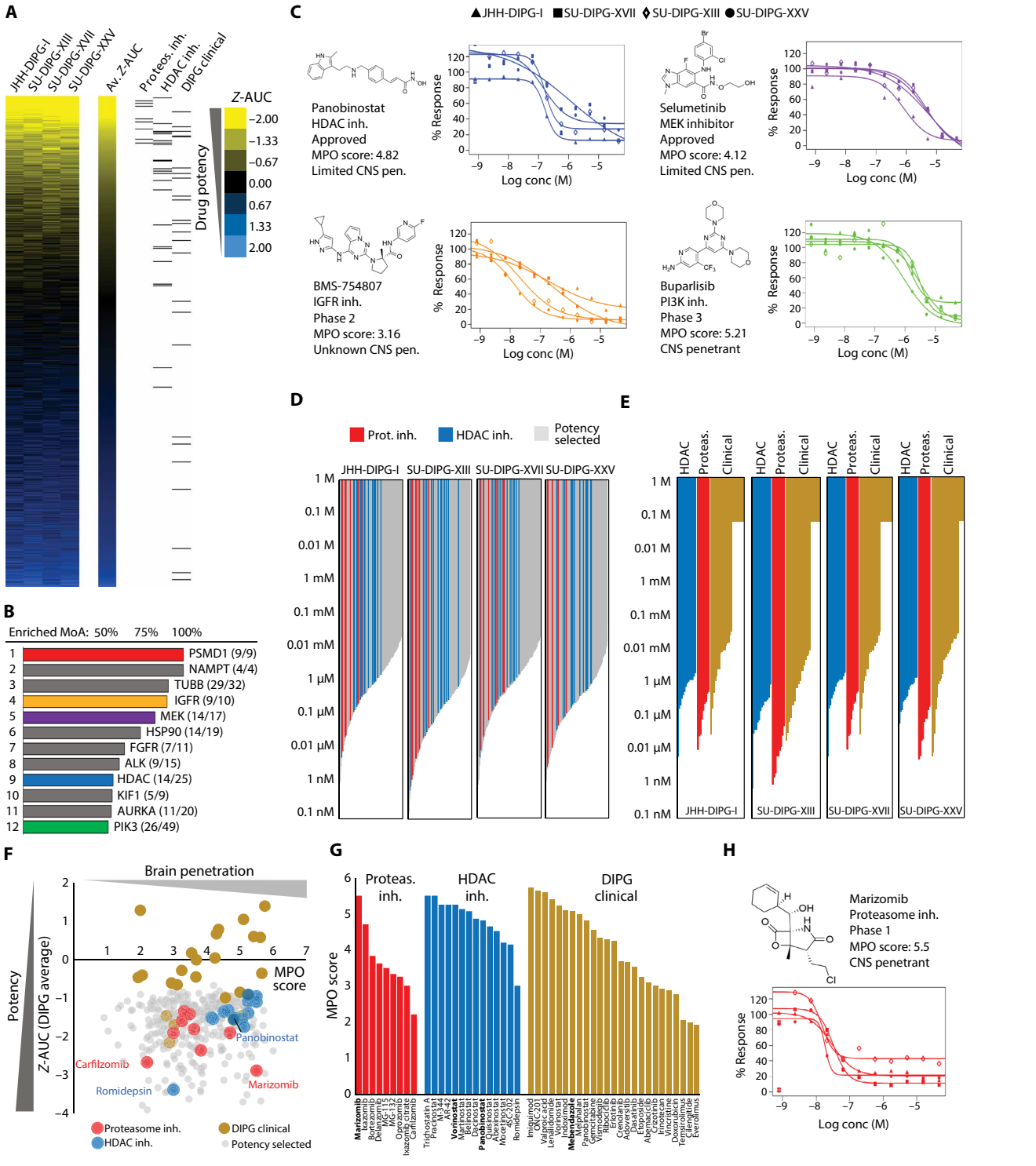

Fig. 1. Drug candidates identified through high-throughput drug screening in DIPG. (**A**) Heat map representation of drug activities for four DIPG cell cultures (JHH-DIPG-1, SU-DIPG-XIII, SU-DIPG-XVII, and SU-DIPG-XXV) screened versus the MIPE 5.0 library. Activity scores are based on *Z*-AUC values. Tick marks on the right side of the plots highlight the relative ranking of proteasome and HDAC inhibitors, as well as the relative rankings of agents in active clinical evaluation in DIPG. (**B**) Mechanistic drug classes enriched among the 371 hits selected on the basis of consistent potency across DIPG cell cultures. Enrichment was defined as number of hits ≥2 and target coverage ≥35%. (**C**) Dose-response curves for selected agents from key enriched mechanistic classes (B) including panobinostat (HDAC), selumetinib (MEK), BMS-754807 (IGFR), and buparlisib (PI3K). (**D**) Potency (AC_{50}) distribution for proteasome (red) and HDAC (blue) inhibitors compared with the 371 potency-selected hits (gray). (**E**) Potency (AC_{50}) distribution for proteasome (red) and HDAC (blue) inhibitors compared with agents in active clinical evaluation in DIPG (mustard). (**F**) For the 371 potency-selected hits, *Z*-AUC values were compared to predicted CNS penetration using MPO scores. The color scheme is the same as in (E). (**G**) Distribution of MPO scores for proteasome inhibitors (red), HDAC inhibitors (blue), and agents in active clinical evaluation in DIPG (mustard). (**H**) Dose-response curves for the proteasome inhibitor marizomib.

Table 1. Cellular cytotoxic response to agents in active clinical evaluation in DIPG (excluding biologics).

Drug name	Mechanism of action	Clinical trial identifier	MPO score*	CNS penetrant†	JHH-DIPG-1‡	SU-DIPG-XIII‡	SU-DIPG-XVII‡	SU-DIPG-XXV‡
Doxorubicin	Topo II inhibitor	NCT02758366§	2.79	Limited‖	1.048 μM	0.934 μM	0.235 μM	1.176 μM
Irinotecan	Topo I inhibitor	NCT03086616¶	2.94	Yes	I.C.	I.C.	0.263 μM	I.C.
Lenalidomide	Cereblon inhibitor	NCT01222754#	5.42	Yes	I.C.	I.C.	I.C.	I.C.
Mebendazole	Tub. depol. inhibitor	NCT01837862**	5.09	Yes	0.468 μM	0.417 μM	0.093 μM	0.331 μM
Vincristine	Tub. pol. inhibitor	NCT01837862**	2.88	Limited	0.029 μM	0.331 μM	0.030 μM	0.030 μM
Abemaciclib	CDK4/6 inhibitor	NCT02644460	3.11	Yes	I.C.	I.C.	I.C.	I.C.
Ribociclib	CDK4/6 inhibitor	NCT03355794††	4.30	Yes	I.C.	I.C.	I.C.	I.C.
Erlotinib	EGFR inhibitor	NCT02233049‡‡	4.25	Limited	I.C.	I.C.	I.C.	I.C.
Dasatinib	Multikinase inhibitor	NCT01644773§§	3.54	Yes	I.C.	I.C.	I.C.	I.C.
Crizotinib	Multikinase inhibitor	NCT01644773§§	3.02	Limited	0.590 μM	0.332 μM	0.468 μM	0.468 μM
Everolimus	mTOR inhibitor	NCT03355794††	1.94	Limited	I.C.	I.C.	I.C.	I.C.
Temsirolimus	mTOR inhibitor	NCT02420613‖‖	2.06	Yes	I.C.	I.C.	I.C.	I.C.
Adavosertib	Wee1 inhibitor	NCT01922076#	3.67	Yes	I.C.	I.C.	I.C.	I.C.
ONC-201	Multiple reports	NCT03416530	5.66	Unknown	I.C.	I.C.	I.C.	I.C.
Valproic acid	HDAC inhibitor	NCT00879437¶¶	5.62	Yes	I.C.	I.C.	I.C.	I.C.
Vorinostat	HDAC inhibitor	NCT01189266#,##	4.82	Unknown	1.481 μM	1.176 μM	1.864 μM	0.833 μM
Panobinostat	HDAC inhibitor	NCT02717455***	5.25	Unknown	0.166 μM	0.166 μM	1.176 μM	0.148 μM

*The CNS MPO scores are based on the design algorithm defined by Wager *et al.* (*18*). †Outcome definitions: "Yes" means that published results confirmed CNS exposure in animal or human studies. "Limited" means that published results suggest no or limited CNS exposure in animal or human studies. "Unknown" means that published results were not available to the best of our knowledge. ‡AC_{50} values are provided for agents with *Z*-AUC values < −0.85 and are based on the NCATS curve generator and are only provided for agents with a curve class designation of −1.1, −1.2, or −2.1 (otherwise noted as I.C. or "incomplete curve") [see (*43*) for curve class definitions]. §NCT02758366 doses doxorubicin using a prolonged infusion alone or in combination with temozolomide or radiation. ‖In NCT02758366, doxorubicin is being dosed using a prolonged, slow infusion, which may increase the CNS exposure. ¶NCT03086616 doses irinotecan using a liposomal formulation administered using convection enhanced delivery. #NCT01189266, NCT01222754, and NCT01922076 are trials combining the named drug with radiation therapy. **NCT01837862 examines mebendazole alone or in combination with vincristine, carboplatin, irinotecan, bevacizumab, and/or temozolomide. ††NCT03355794 examines a combination therapy involving ribociclib and everolimus after radiation therapy. ‡‡NCT02233049 examines combinations of erlotinib, dasatinib, and everolimus. §§NCT01644773 examines a combination therapy involving dasatinib and crizotinib. ‖‖NCT02420613 examines a combination therapy involving temsirolimus and vorinostat. ¶¶NCT00879437 examines a combination therapy involving valproic acid and bevacizumab and radiation. ## Vorinostat is also being explored in NCT02420613. ***NCT03566199 doses panobinostat using a nanoparticle formulation administered using convection enhanced delivery.

with or potentiate marizomib. Selective inhibitors of HDAC6 (for instance, ACY-775 and tubastatin A), a cytoplasmic HDAC implicated in synergy with proteasome inhibitors in multiple myeloma, did not display synergy or potentiation with marizomib in DIPG (*21*, *22*).

To generate a multidimensional drug interaction map, we examined all possible drug-pair interactions among 45 agents (including marizomib and panobinostat) chosen based on single-agent screen outcomes, established synergies from the one-versus-all combination screens, and selected agents of mechanistic interest (Fig. 2E, fig. S2, and table S9 in data file S1). This experiment confirmed synergy between marizomib and panobinostat and established that the included proteasome inhibitors (marizomib, carfilzomib, and ixazomib) were synergistic with the included class I HDAC inhibitors (panobinostat and vorinostat) (Fig. 2F). In addition, panobinostat again synergized with MEK inhibitors (selumetinib and AZD-8330), IGFR inhibitors (BMS-754807), and PI3K inhibitors (buparlisib) (*8*). We also incorporated all drugs in current DIPG clinical evaluation into this screen; combinations of these drugs did not demonstrate notable synergy or potentiation (fig. S3). The correlation heat map of all 45 included agents based on their reciprocal drug-to-drug interaction landscapes (Fig. 2E and fig. S2) enabled us to identify groups of drugs (subclusters) with similar combination profiles. Panobinostat clustered alongside the HSP90 inhibitor alvespimycin (17-DMAG) (group 1),

Table 2. Cellular cytotoxic response to agents with likely CNS exposure and cellular activity in DIPG.

Drug name	Mechanism of action	Development phase*	MPO score†	CNS penetrant‡	JHH-DIPG-1§	SU-DIPG-XIII§	SU-DIPG-XVII§	SU-DIPG-XXV§
Colchicine	Tub. pol. inhibitor	Approved	5.47	Unknown	0.029 μM	0.052 μM	0.030 μM	0.041 μM
Plinabulin	Tub. pol. inhibitor	Phase 3	5.03	Yes	0.052 μM	0.166 μM	0.037 μM	0.047 μM
Combretastatin A-4	Tub. pol. inhibitor	Phase 2	5.36	Yes	0.010 μM	0.018 μM	0.007 μM	0.010 μM
Azixa	Tub. pol. inhibitor	Phase 2	5.08	Yes	0.011 μM	0.009 μM	0.008 μM	0.006 μM
Sepantronium	Survivin inhibitor.	Preclinical	5.63	Unknown	0.104 μM	0.002 μM	0.009 μM	0.026 μM
Marizomib	Proteasome inhibitor	Phase 1	5.50	Yes	0.029 μM	0.014 μM	0.033 μM	0.018 μM
PI-103	PI3K inhibitor	Preclinical	5.40	Unknown	5.254 μM	0.332 μM	0.525 μM	0.186 μM
Daporinad	NAMPT inhibitor	Phase 1	5.09	Yes	0.004 μM	0.002 μM	0.012 μM	0.005 μM
NAMPT-IN-1	NAMPT inhibitor	Preclinical	4.45	Unknown	0.047 μM	0.037 μM	0.263 μM	0.083 μM
GMX-1778	NAMPT inhibitor	Preclinical	5.16	Unknown	0.015 μM	0.008 μM	0.030 μM	0.013 μM
GDC-0623	MEK inhibitor	Phase 1	4.49	Yes	0.105 μM	0.148 μM	0.148 μM	0.331 μM
AZD-8330	MEK inhibitor	Phase 2	4.44	Unknown	0.059 μM	0.132 μM	0.166 μM	0.296 μM
Triptolide‖	XBP inhibitor	Phase 2	5.75	Yes	0.083 μM	0.105 μM	0.186 μM	0.209 μM
Triptonide	XBP inhibitor	Preclinical	6.00	Yes	0.132 μM	0.263 μM	0.296 μM	0.372 μM
Ganetespib	HSP90 inhibitor	Phase 2	5.16	Yes	0.066 μM	0.042 μM	0.037 μM	0.037 μM
HSP-990	HSP90 inhibitor	Preclinical	4.92	Unknown	0.037 μM	0.042 μM	0.030 μM	0.030 μM
NSC-319726	Oxidative stress	Preclinical	5.75	Unknown	0.026 μM	0.024 μM	0.009 μM	0.013 μM
Elesclomol	Oxidative stress	Phase 1	5.21	Unknown	0.005 μM	0.009 μM	0.019 μM	0.019 μM
Dinaciclib	CDK inhibitor	Phase 1	5.20	Yes	0.042 μM	0.037 μM	0.037 μM	0.030 μM
CGP-60474	CDK inhibitor	Preclinical	5.16	Unknown	0.118 μM	0.083 μM	0.132 μM	0.132 μM
SB-1317	CDK inhibitor	Phase 2	4.54	Unknown	0.166 μM	0.132 μM	0.083 μM	0.093 μM
Podofilox	Topo II inhibitor	Approved	5.27	Unknown	0.030 μM	0.030 μM	0.042 μM	0.047 μM

Notes: Agents with an MPO score above 4.0 and an average *Z*-AUC below −1.9. *Highest achieved clinical phase in any indication at the time of publication. †The CNS MPO scores are based on the design algorithm defined by Wager *et al.* (*18*). ‡Outcome definitions: "Yes" means that published results confirmed CNS exposure in animal or human studies. "Unknown" means that published results were not available to the best of our knowledge. §AC_{50} values are provided for agents with *Z*-AUC values < −0.85 and are based on the NCATS curve generator and are only provided for agents with a curve class designation of −1.1, −1.2, or −2.1 [see (*43*) for curve class definitions]. ‖This agent is in active clinical evaluation as a prodrug named Minnelide.

suggesting potential interplay between HDAC and HSP90. Proteasome inhibitors (ixazomib, carfilzomib, and marizomib) clustered together and demonstrated a similar combination pattern with the vacuolar-type H^+-ATPase (adenosine triphosphatase) inhibitor bafilomycin A (group 2). Several signaling inhibitors (group 3; for instance, BMS-754807, buparlisib, and selumetinib) clustered together alongside modulators of tubulin function (for instance, vincristine, plinabulin, and mebendazole). Several drugs within this signaling group showed mutual synergy among each other (table S9), supporting the idea that IGFR, PI3K, and MEK signaling cooperate to sustain DIPG viability. Because our screening data were generated using an adenosine triphosphate (ATP)–dependent assay (CellTiter-Glo) to measure cell viability, we also repeated key single-agent and combination screening experiments using alternative assays measuring live-cell protease activity (glycylphenylalanyl-aminoflurocoumarin substrate) and caspase activation (Caspase-Glo 3/7). These data broadly confirm all CellTiter-Glo outcomes. These collective screening experiments highlight several potentially exploitable mechanistic vulnerabilities in DIPG.

Panobinostat and marizomib emerge as a promising combination from in vitro evaluation of top combination candidates across representative patient-derived DIPG cultures

Given the ongoing clinical trials of the HDAC inhibitor panobinostat and its prominence as a top hit throughout our screens, we evaluated four drugs (marizomib, selumetinib, BMS-754807, and buparlisib) in combination with panobinostat against six patient-derived DIPG cell cultures representing the three major genetic subtypes (H3.3K27M: SU-DIPG-VI, SU-DIPG-XIII, and SU-DIPG-XVII; H3.1K27M: SU-DIPG-IV and SU-DIPG-XXI; H3 wild type: VUMC-DIPG-10; full culture data are shown in table S10 in data file S1). We generated

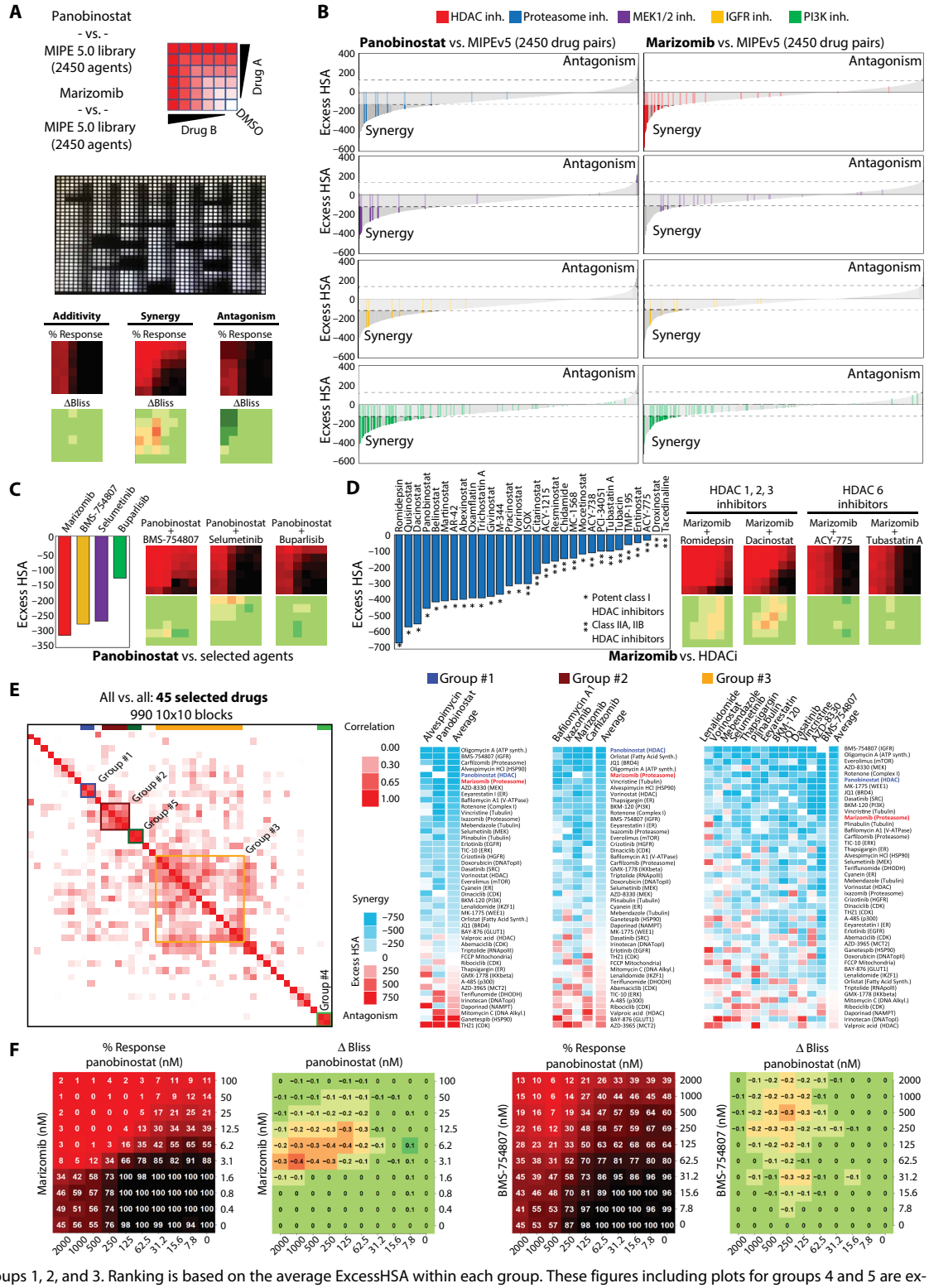

Fig. 2. Synergistic drug-drug interactions in DIPG identified via HTS-enabled combination drug screening. (**A**) Schematic layout of the drug-versus-all screen for panobinostat and marizomib versus the entire MIPE 5.0 library. Top: Each drug pair was tested in a 6 × 6 matrix block, reflecting five doses plus DMSO control for each individual matrix block. Middle: An exemplar 1536 plate containing 6 × 6 blocks. Bottom: Examples of percent response and ΔBliss heat maps for additivity, synergy, or antagonism outcomes. (**B**) The entire panobinostat (left panels) and marizomib (right panels) drug-versus-all screen results were ranked by synergy, as assessed by the ExcessHSA metric (gray). Each panel highlights drugs from key mechanistic classes including HDAC, proteasome, MEK, IGFR, and PI3K inhibitors. (**C**) Left: ExcessHSA values for the combination of panobinostat with the proteasome inhibitor marizomib, the IGFR inhibitor BMS-754807, the MEK inhibitor selumetinib, and the PI3K inhibitor buparlisib. Right: %Response and ΔBliss heat maps for panobinostat with BMS-754807, selumetinib, or buparlisib. (**D**) Left: Thirty HDAC inhibitors from the MIPE 5.0 library were ranked on the basis of the ExcessHSA values when combined with marizomib. Class I (*) and class II/III (**) HDAC inhibitors are highlighted. Right: %Response and ΔBliss heat maps, for example, class I pan-HDAC inhibitors (romidepsin and dacinostat) or class II HDAC6 inhibitors (ACY-775 and tubastatin A). (**E**) Left: Correlation heat map of the 45-drug all-versus-all combination screen. Subgroups of drugs with similar combination profiles are highlighted (group 1: blue; group 2: brown; group 3: orange; group 4: light green; group 5: dark green). Right: Original ExcessHSA values for groups 1, 2, and 3. Ranking is based on the average ExcessHSA within each group. These figures including plots for groups 4 and 5 are expanded in fig. S2. (**F**) The 10 × 10 %Response heat maps and ΔBliss heat maps for the combinations of panobinostat with either marizomib or BMS-754807.

drug dose-response curves for these candidate agents alone and with 25 nM panobinostat, a sub-IC_{50} (half maximal inhibitory concentration) dose, to examine the drug interaction across cultures (Fig. 3A). Although all four candidates demonstrated a shift of their dose-response curves when combined with panobinostat, marizomib and BMS-754807 exhibited substantial decreases in cell viability in all cultures tested at concentrations achievable in the pons after systemic administration [IC_{50} < 30 nM; for marizomib, intravenous

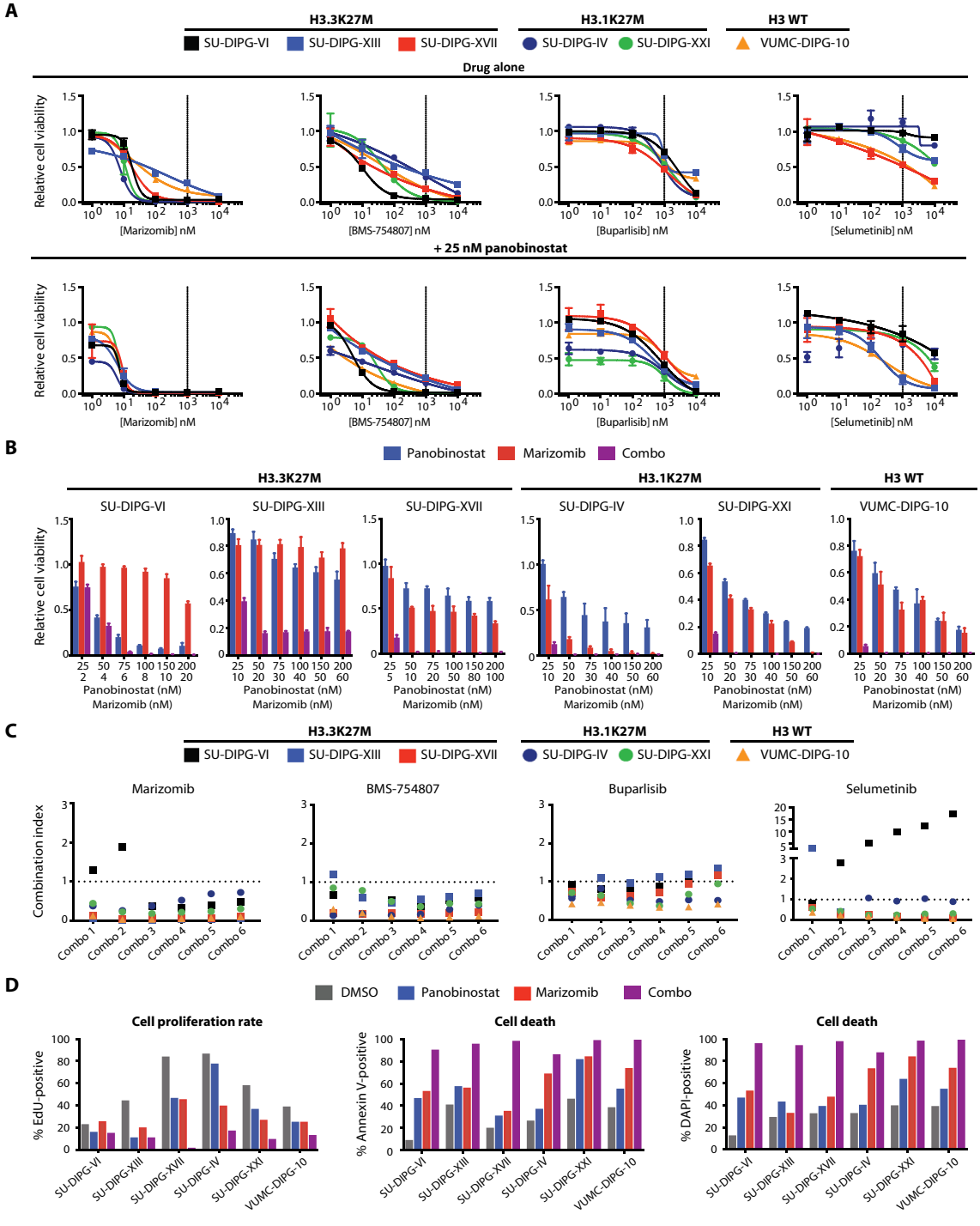

Fig. 3. In vitro validation of top drug combinations across representative DIPG cell cultures. (**A**) Dose-response curves of cell viability of patient-derived DIPG cell cultures, as measured by CellTiter-Glo and compared to DMSO control after 72-hour exposure to top candidate therapeutic agents marizomib, BMS-754807, buparlisib, and selumetinib alone (top) or with 25 nM panobinostat (bottom). Vertical line is at 1000 nM (1 μM), representing an approximate range for achievable concentrations in vivo. WT, wild type. (**B**) Cell viability compared to DMSO control after 72-hour exposure of six patient-derived DIPG cell cultures to varying doses of panobinostat (blue), marizomib (red), or both (purple). Similar measurements for the other top drug combination candidates can be found in fig. S4A. (**C**) Calculated median effect drug synergy CI scores (Biosoft CalcuSyn 2.0) across doses for each of the four candidate drug combinations [individual viability measurements in (B) and fig. S4A]. Horizontal dashed line indicates a CI = 1, where points below the line indicate synergy and points above the line indicate antagonism. (**D**) Cell proliferation as measured by flow cytometric analysis of EdU incorporation (left) and cell death as measured by surface labeling of Annexin V (middle) and permeability to DAPI (right) of six patient-derived DIPG cell cultures. For EdU analysis, cells were incubated with DMSO vehicle (control; gray), panobinostat (blue), marizomib (red), or combination of panobinostat and marizomib (combo; purple) for 16 hours and then exposed to 10 μM EdU for 24 hours before analysis. For Annexin V and DAPI analysis, cells were incubated for 48 hours before analysis. Individual flow cytometry histograms can be found in fig. S4B.

administration has been shown to have good blood-brain barrier penetrance (*19*, *20*, *23*); for BMS-754807, intratumoral concentrations of ~40 nM were achieved in vivo (*24*)]. Buparlisib, in the presence of 25 nM panobinostat, resulted in an IC_{50} ranging from 430 to 1041 nM. Selumetinib exhibited divergent effects across the cultures tested, including a paradoxical increase in cell viability in SU-DIPG-IV such that a dose-response curve could not be calculated.

We next measured DIPG cell viability across different drug doses or combinations in each culture (Fig. 3B and fig. S4A). We used the CalcuSyn 2.0 software (Biosoft) to establish conventional metrics for each drug combination (*25*). This demonstrated consistent synergy [combination index (CI) < 1] between panobinostat and marizomib, panobinostat and BMS-754807, and, to a lesser degree, panobinostat and buparlisib (Fig. 3C). The combination of panobinostat and selumetinib demonstrated synergy in four of six patient cultures, but no synergy in SU-DIPG-IV and antagonistic effects on SU-DIPG-VI. Because of the concentration required for cell killing and the lower degree of synergy, we removed buparlisib from subsequent analyses.

To assess cell proliferation and cell death in response to drug treatment, we performed flow cytometry analysis of 5-ethynyl-2′-deoxyuridine (EdU) incorporation, Annexin V staining, and 4′,6-diamidino-2-phenylindole (DAPI) incorporation. Panobinostat and marizomib together, compared to either drug alone, had robust effects on cell proliferation and cell death (Fig. 3D and fig. S4B). Combining panobinostat and BMS-754807 also showed added but less pronounced effects (fig. S5, A and B). Evaluation of panobinostat and selumetinib again demonstrated divergent effects across cultures, including an increase in EdU incorporation in SU-DIPG-IV and a decrease in Annexin V staining in SU-DIPG-VI (fig. S5, C and D).

Panobinostat and marizomib demonstrate efficacy as combination treatment in patient-derived DIPG xenografts

We evaluated the remaining combinations in vivo (panobinostat with marizomib, BMS-754807, or selumetinib). We first tested these candidates as single agents in an orthotopic patient-derived xenograft model engineered to express firefly luciferase (SU-DIPG-VI). In vivo bioluminescence imaging was performed immediately before drug or vehicle control administration to assess baseline tumor burden. Intravenous marizomib treatment led to a significant decrease in tumor burden at each of two different doses measured 4 weeks after treatment initiation (top, $P < 0.05$; bottom, $P < 0.01$; Fig. 4A). Oral treatment with BMS-754807 and selumetinib (fig. S6A) did not show efficacy as single agents.

Using an aggressive patient-derived xenograft model (SU-DIPG-XIII-P*, a subclone of the patient-derived SU-DIPG-XIII pons culture that demonstrates more aggressive growth in vivo, enabling survival analysis) to evaluate the effects of combination treatment, we found that the combination of panobinostat and marizomib, alternating weeks, led to an increase in median survival (top, $P < 0.01$; Fig. 4B). Single-agent treatment with panobinostat or marizomib led to smaller increases in overall survival. To control for the additional overall dosing of the combination arm, we tested a second cohort in which the single-agent arms received twice the dosing of their respective drugs (Fig. 4B). Combination treatment again increased overall survival ($P < 0.01$). Panobinostat and marizomib again led to smaller increases in overall survival. To assess whether these agents cause acute neurotoxicity, we treated another cohort of mice and evaluated apoptosis in normal brain tissue by cleaved caspase-3 (CC3) immunostaining 24 hours after vehicle control, panobinostat, or marizomib administration. We found negligible cell death in normal brain tissue and no difference between treatment and control groups (fig. S6B).

We next tested BMS-754807 and selumetinib in combination with panobinostat using the SU-DIPG-XIII-P* xenograft model (fig. S6C). Survival was not extended in the BMS-754807 treatment cohort. In the selumetinib-treated cohort, only the single-agent panobinostat-treated group exhibited modestly increased survival, whereas single-agent selumetinib-treated mice demonstrated no change from vehicle-treated controls. Alarmingly, combination-treated mice demonstrated no change in survival despite receiving the same amount of panobinostat as the single-arm control, suggesting that selumetinib may abrogate the effect of panobinostat alone.

Panobinostat and marizomib demonstrate efficacy in other patient-derived DMG xenograft models

DIPG was recently reclassified with spinal cord and thalamic gliomas that bear the signature H3K27M mutation (*6*, *7*). Using patient-derived spinal cord glioma (SU-pSCG-1) and thalamic glioma (QCTB-R059) culture models, we evaluated whether single-agent panobinostat treatment also demonstrates efficacy across nonpontine DMGs. In vitro, treatment with panobinostat demonstrated efficacy at nanomolar concentrations (SU-pSCG-1, IC_{50} = 29.4 nM; QCTB-R059, IC_{50} = 40.7 nM; fig. S7, A and B). To evaluate in vivo efficacy, we xenografted SU-pSCG-1 into the medulla or QCTB-R059 into the thalamus. Subsequent bioluminescence imaging before and after 1 week of panobinostat treatment demonstrated reduction in orthotopic tumor progression in SU-pSCG-1 (brain, $P < 0.05$; spinal cord, $P < 0.05$; fig. S7C) and QCTB-R059 ($P < 0.0005$; fig. S7D) xenografts.

We next assessed the combination of marizomib with panobinostat against nonpontine DMGs. In vitro, the addition of 25 nM panobinostat lowered the IC_{50} of marizomib to low nanomolar concentrations in SU-pSCG-1 (2.468 nM) and QCTB-R059 (5.918 nM) (fig. S7, E and F). We also measured tumor cell viability at different drug doses or combination (fig. S7, G and H) and calculated drug synergy using the CalcuSyn 2.0 software (fig. S7I). In both models, panobinostat and marizomib demonstrated synergy at all doses tested.

To assess combination efficacy in vivo, we orthotopically xenografted QCTB-R059 cells into the thalamus. In vivo bioluminescence imaging was performed directly before treatment and 4 weeks after treatment, demonstrating a significant response (panobinostat 2.8-fold decrease, $P < 0.05$; marizomib 2.6-fold decrease, $P < 0.05$; combination 4.6-fold decrease versus control, $P < 0.01$; Fig. 4C). To assess whether these agents cause neurotoxicity, we evaluated tumor and normal cell apoptosis by CC3 immunostaining in these mice after 4 weeks of treatment. We observed an increase in tumor cell CC3 staining in all treatment conditions (fig. S8A), but found negligible CC3 in nontumor cells (fig. S8B), supporting the idea that long-term treatment is not associated with evident toxicity to normal brain cells. These data support panobinostat and marizomib as an effective combinatorial strategy across DMGs originating in both pontine and nonpontine anatomical locations.

Combination-treated DMG cells exhibit altered transcriptional identity

To explore the mechanism underlying synergy between panobinostat and marizomib in DMG cells, we performed RNA sequencing on SU-DIPG-XIII sampled after 16 hours of exposure to dimethyl

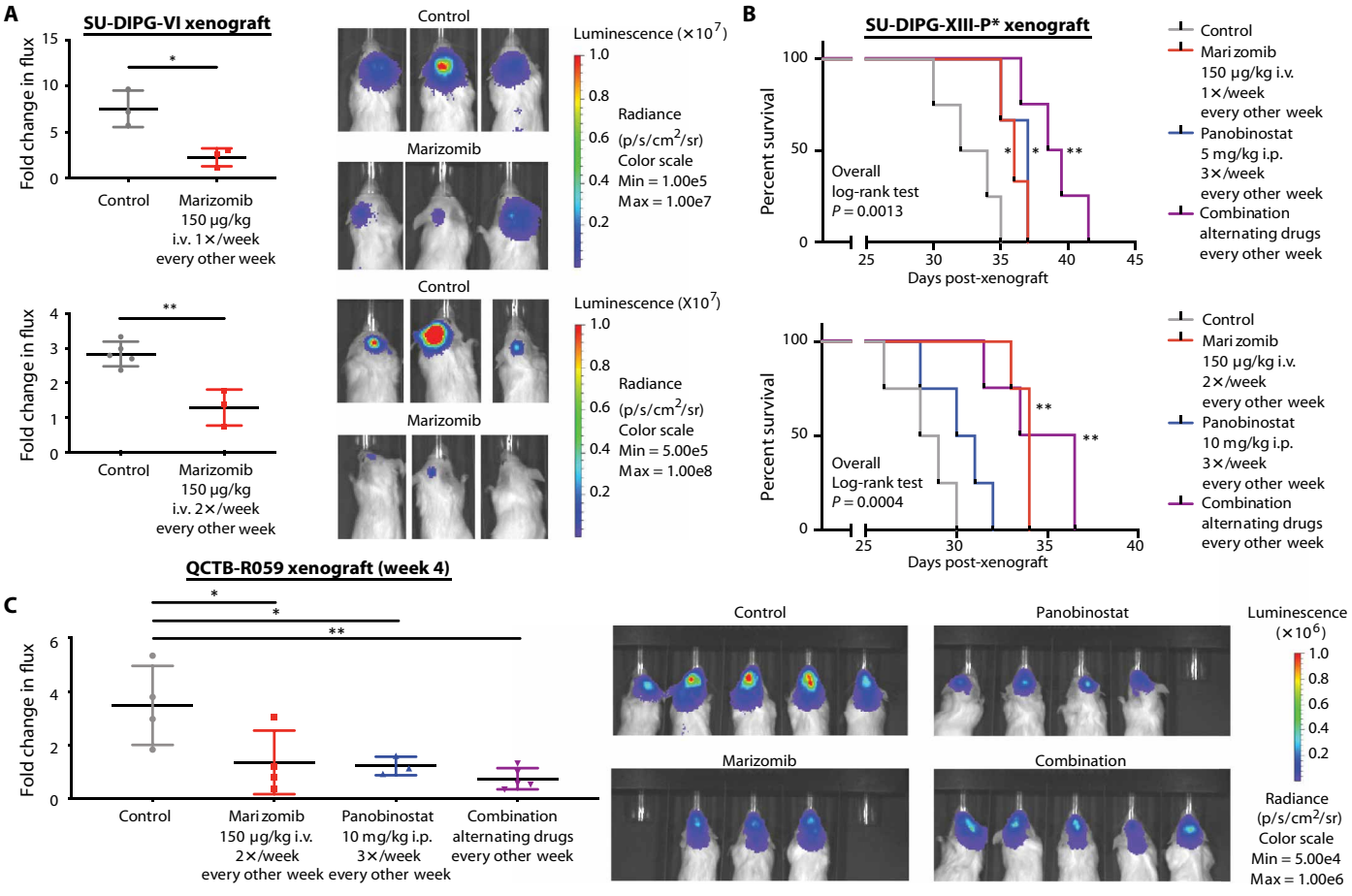

Fig. 4. Panobinostat and marizomib in xenograft models of DIPG and other DMGs. (**A**) In vivo bioluminescence imaging of SU-DIPG-VI GFP-luc xenografts after 4 weeks of treatment with marizomib at 150 µg/kg once every 2 weeks (top; $n = 3$ vehicle controls and $n = 3$ treated mice) or 150 µg/kg twice every 2 weeks (bottom; $n = 5$ vehicle controls and $n = 3$ treated mice; two-tailed t test). i.v., intravenously. (**B**) Overall survival of SU-DIPG-XIII-P* xenografted mice treated with vehicle, panobinostat alone (top: 5 mg/kg; bottom: 10 mg/kg; three times per week, every other week), marizomib alone (top: 150 µg/kg, one time per week; bottom: two times per week, every other week), or combination (panobinostat: 5 mg/kg, three times per week, every other week; marizomib: 150 µg/kg, one time per week, every other week in both cohorts; log-rank test). (**C**) In vivo bioluminescence imaging of QCTB-R059 GFP-luc xenografts after 4 weeks of treatment with vehicle control, panobinostat (5 mg/kg; three times weekly, every other week), marizomib (150 µg/kg; once weekly, every other week), or combination of panobinostat and marizomib (alternating every week). One-way ANOVA with Tukey's multiple comparisons test. *$P < 0.05$ and **$P < 0.01$.

sulfoxide (DMSO), panobinostat, marizomib, or two combination doses (Fig. 5, A and B). Principal components analysis of these data demonstrated that panobinostat and marizomib affect an orthogonal gene set while also displaying concordance in terms of the overall gene universe change in expression directionality (Fig. 5A and fig. S9, A and B). Direct comparison of the two combination doses did not demonstrate a pronounced difference (fig. S9B). We next performed gene set enrichment analysis (GSEA) of each treatment with respect to DMSO (*26*). Enriched gene sets were annotated for each comparison and analyzed by unsupervised hierarchical clustering of their normalized enrichment scores, demonstrating substantial overlap across comparisons. For example, cell cycle and oxidative phosphorylation gene sets were consistently down-regulated and apoptosis-related genes were consistently up-regulated by all treatment groups (Fig. 5C and figs. S9, C and D, and S10). An unfolded protein response (UPR) gene set was unaffected by treatment with panobinostat but up-regulated by marizomib. Up-regulation of the UPR response was further potentiated by combination treatment. The UPR pathway was also identified when genes affected only by combination drug treatment were functionally categorized with Cytoscape enrichment maps (Fig. 5D) (*27*, *28*). Leading-edge analysis from the GSEA UPR gene set highlighted genes that were strongly up-regulated only in combination-treated cells (Fig. 5E). We repeated RNA sequencing experiments on two additional patient-derived cell cultures (SU-DIPG-VI and QCTB-R059) (fig. S11A). These data demonstrated overlapping signatures with the SU-DIPG-XIII dataset (fig. S11B). Up-regulation of the UPR gene set in marizomib and combination-treated cells was a consistent finding across patient-derived cultures (fig. S11, C and D).

Western blot analysis of treated SU-DIPG-XIII cells showed increased amounts of key modulators of the UPR such as the endoplasmic reticulum (ER) chaperone protein BiP and the ER stress–associated transcription factor CHOP in combination-treated cells (Fig. 5F and fig. S12A). Western blot analyses also showed increased apoptotic markers, as assessed by CC3 and cleaved PARP [poly(adenosine diphosphate–ribose) polymerase], in combination-treated cells (Fig. 5F and fig. S12A). Treatment with marizomib, either alone or in combination with panobinostat, resulted in increased ubiquitinated proteins and accumulation of the proliferation inhibitor p21 and

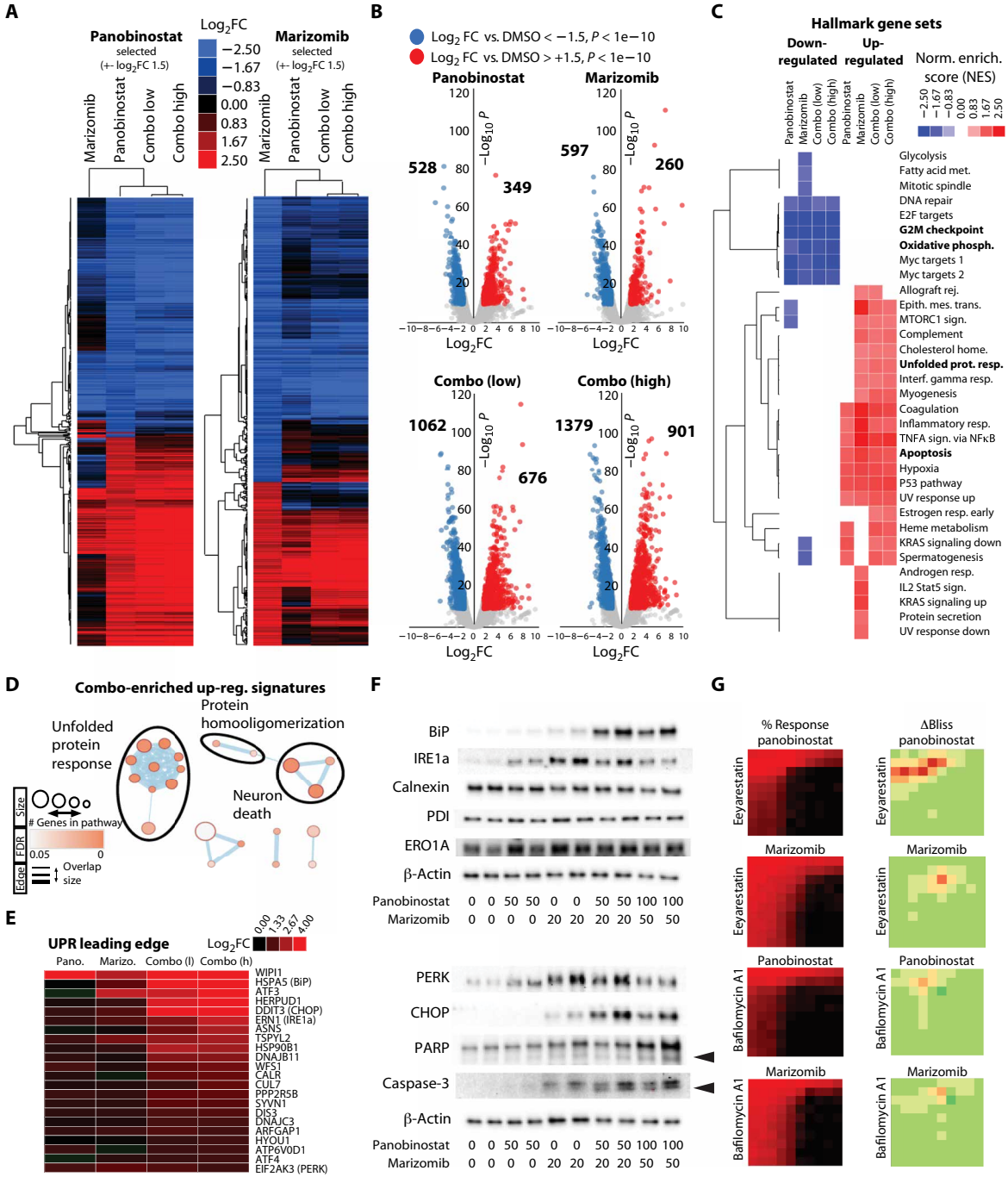

Fig. 5. RNA sequencing analysis of the combination of panobinostat and marizomib in SU-DIPG-XIII cells. (**A**) Heat map representations of the $\log_2$ gene expression changes ($\log_2$FC) after treatment of SU-DIPG-XIII with 50 nM panobinostat, 20 nM marizomib, or two combination doses (50 nM + 20 nM or 100 nM + 50 nM, panobinostat and marizomib, respectively). Differentially expressed genes were selected on the basis of either panobinostat versus DMSO (left) or marizomib versus DMSO (right) comparisons, and heat maps depicting all four treatments were then generated by unsupervised hierarchical clustering. (**B**) Volcano plot of each individual treatment set with respect to the DMSO control. Significantly down- or up-regulated genes are highlighted in blue or red, respectively. (**C**) A fold change preranked list of each treatment versus DMSO was used to run GSEA against the Hallmark (shown here) and Reactome (fig. S9C) gene sets. Unsupervised hierarchical clustering of normalized enrichment scores (NES) was used to generate a comprehensive heat map visualization of the functional transcriptional outputs of the four treatment sets. (**D**) Cytoscape enrichment map visualization of top gene programs represented by significantly up-regulated genes present in combination-low treated cells but not either single-agent treated condition. Node size represents number of genes, node color represents significance [false discovery rate (FDR)], and edge thickness represents number of shared genes. Clustered gene programs are labeled. (**E**) Gene expression changes for the "leading-edge" genes from the Reactome-UPR gene set. Leading selection and ranking were based on the combo-high (h) treatment set. (**F**) Western blot analysis of the indicated ER stress/UPR or apoptosis biomarkers is shown for all four treatment sets. Black triangles denote cleaved PARP and CC3. β-Actin was used as a loading control. (**G**) %Response and ΔBliss heat maps are shown for the combination of either panobinostat or marizomib with the ER modulators eeyarestatin and bafilomycin A1.

the heat shock factor HSP70 (fig. S12B). Treatment with panobinostat, either alone or in combination with marizomib, resulted in increased H3 acetylation and α-tubulin acetylation (fig. S12C). On the basis of the UPR outcomes, we incorporated several ER modulators into follow-up experiments, including bafilomycin A, the sarco/ER Ca^{2+} ATPase (SERCA) inhibitor thapsigargin, the ER protein transport inhibitor brefeldin A, and the ER-associated protein degradation inhibitor eeyarestatin. These agents exacerbated the cytotoxic potential of panobinostat, marizomib, or the combination of these agents (Fig. 5G and fig. S12D).

Panobinostat and marizomib combination-treated DIPG cells undergo metabolic collapse

Both GSEA and Cytoscape enrichment map analyses identified transcriptional down-regulation of cellular metabolism and respiration in combination-treated cells (Figs. 5C and 6, A and B, and figs. S11A and S13, A and B). The oxidative phosphorylation gene set was consistently down-regulated by combination treatment. Moreover, analysis of oxidative phosphorylation leading-edge genes demonstrated effects mostly on the complex I gene family {NADH [reduced form of NAD^+ (nicotinamide adenine dinucleotide)]:ubiquinone oxidoreductase subunits (NDUFs)} and electron transport chain (ETC) modulators (for example, ATP5J2) (Fig. 6B and figs. S13 and S14A). In the 45-drug all-versus-all screen, combining ETC inhibitors (the complex I inhibitor rotenone and the H^+-ATP synthase inhibitor oligomycin) with glycolytic flux inhibitors (the GLUT1 inhibitor BAY-876 and the MCT2 inhibitor AZD-3965) demonstrated the strongest synergy (Fig. 6C and fig. S14B). These two classes formed well-resolved subclusters in the all-versus-all correlation heat map (Fig. 2E). The ETC inhibitors (group 4) were antagonistic among themselves but had similar synergistic profiles with most agents tested, suggesting that inhibition of mitochondrial respiration generally increases the susceptibility of DIPG cells to cytotoxic agents (Fig. 6D, left). Conversely, glycolytic flux inhibitors (group 5) had notable synergy with only ETC drugs and no other meaningful drug interaction (Fig. 6D, right).

To better define the metabolic consequences induced by panobinostat and marizomib, we performed liquid chromatography/mass spectrometry analysis of DMG cellular metabolites across representative patient-derived cell cultures. Unsupervised hierarchical clustering of the fold change of profiled metabolites compared to DMSO control demonstrated a distinct profile in combination-treated cells (Fig. 6E and fig. S14, C and D). Key divergent metabolites included a combination-specific increase in oxidized glutathione (GSSG) and decrease in reduced glutathione (GSH), suggesting oxidative stress as a mechanistic driver of the combination-specific cytotoxicity (fig. S14, C and D). To test this possibility, we repeated key combination studies with the reactive oxygen species (ROS) scavenger *N*-acetylcysteine. However, this did not rescue cell viability, suggesting that ROS induction is not a causal element of drug combination–driven cytotoxicity (fig. S15). Another key divergent metabolite was a combination-specific up-regulation of 3-phosphoglyceric acid (3-PG), which can indicate pentose phosphate pathway arrest and decreased glycolytic flux. In addition, down-regulation of NAD^+ and accumulation of citric acid cycle members, hallmarks of general mitochondrial dysfunction, were more pronounced in combination-treated cells (Fig. 6F and figs. S14, C and D, and S16A). These results prompted us to analyze mitochondrial respiration in DMG cells after drug exposure. Using Seahorse-based assays, we observed marked decreases in basal cellular respiration and spare respiratory capacity of combination-treated cells (Fig. 6G and fig. S16B).

We hypothesized that the combination-induced cytotoxicity could be due to metabolic catastrophe mirroring the acute toxicity observed when combining ETC inhibitors and glycolytic flux modulators (Fig. 6, C and D). To test this, we manipulated cellular NAD^+ concentrations through exogenous addition of nicotinamide mononucleotide (NMN), the metabolic precursor to NAD^+, or daporinad, a nicotinamide phosphoribosyltransferase (NAMPT) inhibitor. First, we demonstrated in SU-DIPG-XIII cells that NMN increases cellular NAD^+, daporinad reduces cellular NAD^+, and NMN and daporinad together result in normalized NAD^+ concentrations (fig. S16C). Daporinad alone increased cell death, and as expected, this effect was reversed by NMN supplementation (fig. S16C). In combination-treated cells, NMN supplementation restored physiological NAD^+ concentrations, whereas daporinad exacerbated the combination-induced effect on cellular NAD^+ (Fig. 6H). Consistently, daporinad administration increased the cytotoxicity of the combination treatment, and NMN supplementation reversed this effect. Critically, NAD^+ concentration appears to inversely correlate with DIPG cell viability, and NMN supplementation completely blocked the combination-induced cytotoxicity (Fig. 6I). Given the profound rescue by NMN supplementation, we repeated this experiment on five representative patient-derived DMG cell cultures: H3.3K27M DIPG (SU-DIPG-VI), H3.1K27M DIPG (SU-DIPG-XXI), H3WT DIPG (VU-DIPG-10), H3.3K27M spinal cord glioma (SU-pSCG-1), and H3.3K27M thalamic glioma (QCTB-R059). We found that NMN robustly blocks the combination-induced cytotoxicity in five of six tested cultures and reduces the combination-induced cytotoxicity in the last culture (QCTB-R059) (fig. S16D). Cytotoxicity induced by the tubulin polymerization inhibitor vincristine, which does not act through metabolic pathways, was not blocked by NMN supplementation (fig. S16E). Together, these findings demonstrate that both H3K27M and H3 wild-type DMG cells are highly sensitive to metabolic perturbations and that metabolic dysfunction is a causal component of the cytotoxic effects of the panobinostat and marizomib combination in DMG.

DISCUSSION

The urgent need for effective therapeutic strategies for DMGs is highlighted by the lack of improvement in overall survival despite decades of clinical trials. The recent development of patient-derived DMG cell cultures along with the comprehensive genomic characterization of pediatric brain tumors has moved us beyond empiric testing to targeted drug discovery for this fatal disease. Here, we report a comprehensive single-agent and combination drug screen against DIPG, with data publicly available to the research community to guide preclinical exploration of promising therapies for DMG and provide rationale for clinical trial design. Furthermore, we demonstrate that the combination of HDAC inhibition and proteasome inhibition has potent synergy and represents a promising clinical strategy for treating DMGs. H3.3K27M, H3.1K27M, and H3WT gliomas appear to respond similarly to this combination, suggesting broad utility across subgroups of DMGs. Last, we find that this synergy is driven by a metabolic crisis within DMG cells, uncovering a metabolic sensitivity in DMG.

Caveats about the patient-derived models used here include limited models in which assessing survival is feasible. Patient-derived models

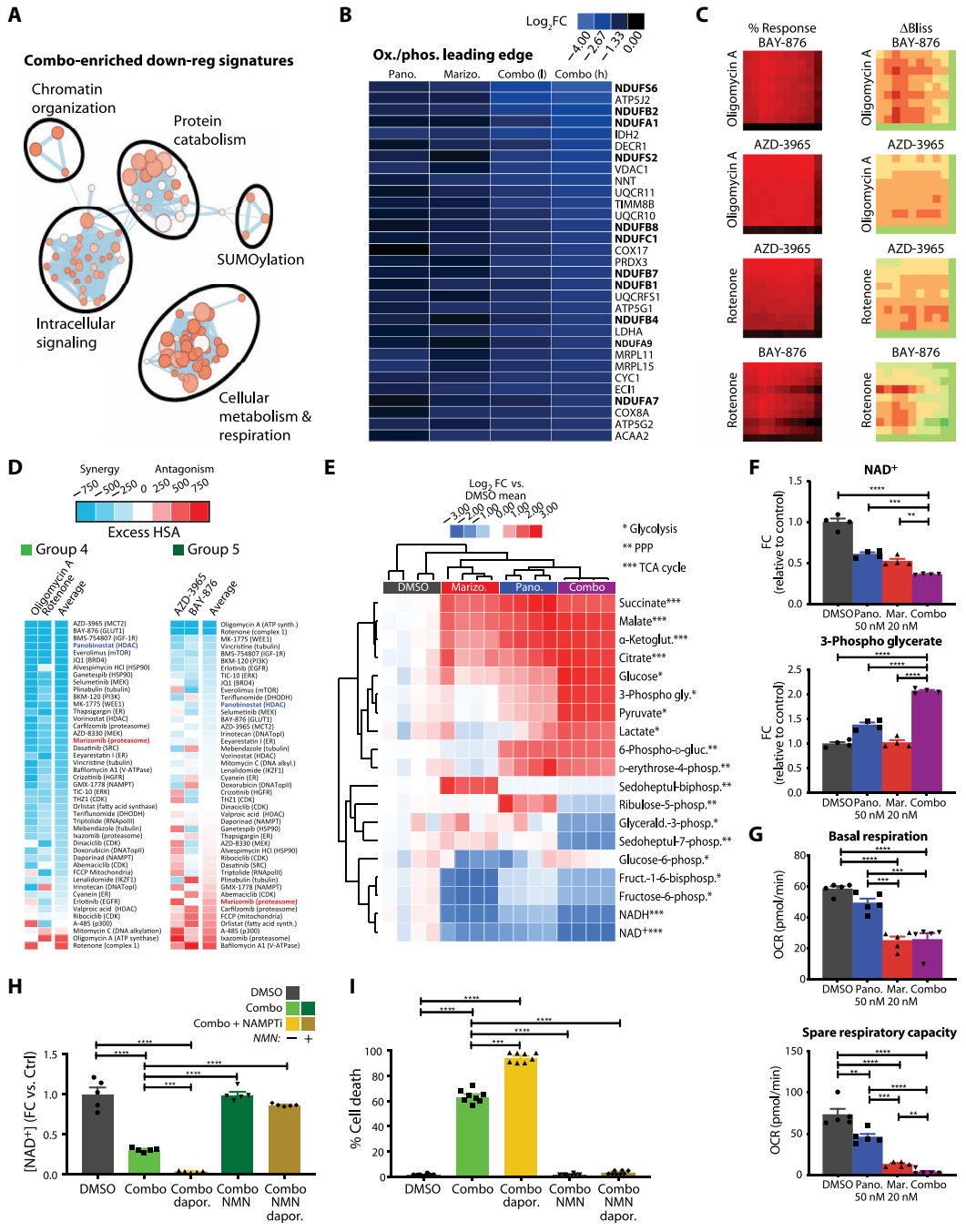

Fig. 6. Targeted metabolic profiling of the combination of panobinostat and marizomib in SU-DIPG-XIII cells. (**A**) Cytoscape enrichment map visualization of top gene programs represented by significantly down-regulated genes present in combination-low treated cells but not either single-agent treated condition. Node size represents number of genes, node color represents significance (false discovery rate), and edge thickness represents number of shared genes. Clustered gene programs are labeled. (**B**) Gene expression changes for the leading-edge genes from the Hallmark-Oxidative Phosphorylation gene set. Leading selection and ranking were based on the combo-high treatment set. Complex I gene family members (NDUFs) are bolded. (**C**) %Response and ΔBliss heat maps highlighting the "synthetic lethality" for the combination of ETC inhibitors (the complex I inhibitor rotenone or the H^+-ATP synthase inhibitor oligomycin A) with glycolytic flux inhibitors (the GLUT1 inhibitor BAY-876 or the MCT2 inhibitor AZD-3965). (**D**) ExcessHSA values for well-resolved subclusters of ETC (group 4) or glycolytic flux (group 5) inhibitors originally identified in the correlation heat map for the 45-drug all-versus-all screen (Fig. 2E). Ranking is based on the average ExcessHSA within each group. This plot is expanded in fig. S2C. (**E**) Heat map displaying unsupervised hierarchical clustering of fold change of metabolites with respect to DMSO control, quantified by liquid chromatography/mass spectrometry. (**F**) Relative abundance of NAD^+ and 3-phosphoglycerate in each treatment set with respect to the DMSO control. (**G**) Basal respiration and spare respiratory capacity, as assessed by Seahorse experiments, are reported for each treatment set. (**H**) Relative NAD^+ concentration in combination-treated (24 hours) cells with respect to the DMSO control, in the presence or absence of the NAD^+ precursor NMN, the NAMPT inhibitor daporinad, or both. (**I**) Cell death in combination-treated (24 hours) cells with respect to DMSO control in the presence or absence of NMN, daporinad, or both. $^{**}P < 0.005$, $^{***}P < 0.0005$, and $^{****}P < 0.0001$.

of DMG typically require many months for lethality, limiting survival studies to only unusually aggressive patient-derived xenograft (PDX) models such as SU-DIPG-XIII-P*. It should be noted that the in vivo efficacy demonstrated here is modest. This is consistent with the clinical intractability of the disease, for which any measurable prolongation of survival would be a step in the right direction. Ultimately, curative therapy for DMGs will likely require a multipronged approach, targeting cell-intrinsic vulnerabilities as described here, together with targeting key microenvironmental dependencies (*29*) and leveraging immunotherapeutic opportunities (*30*).

The combination of HDAC and proteasome inhibition has been pursued as a therapeutic strategy in other tumors, most notably multiple myeloma, with demonstrated safety and tolerability (*31*–*33*). In adult glioma cell lines, an in vitro study described synergy between the HDAC inhibitor vorinostat and the proteasome inhibitor bortezomib (*34*). Several mechanisms have been proposed for the

synergy between HDAC and proteasome inhibitors, including the combination of HDAC6-mediated aggresome formation and proteasomal degradation resulting in defective protein catabolism, whereas other studies have implicated HDAC6-independent mechanisms (*21*, *22*, *35*, *36*). Our marizomib-based combination assessments revealed class I HDAC inhibitor–specific synergy in DIPG. Similar to previous reports, we observe that combining HDAC and proteasome inhibitors (for example, panobinostat and marizomib) results in up-regulation of the UPR at the gene expression and protein levels.

We noted several other acute changes to gene expression after panobinostat and marizomib treatments. Among the most notable features was the combination-specific down-regulation of metabolism-related genes. The altered metabolic state of cancer cells is well studied, and targeting key metabolic vulnerabilities in cancer is emerging as an attractive therapeutic modality (*37*, *38*). Here, we found that selected modulators of mitochondrial respiration and glycolytic flux together create a lethal state in DMG. Furthermore, combining panobinostat and marizomib alters the metabolic profile of DMG cells in a manner distinct from either single-agent treatment, including a substantial reduction in NAD^+. Critically, restoring NAD^+ concentrations with NMN supplementation completely mitigates the combination-induced cytotoxicity, whereas NAD^+ depletion via the NAMPT inhibitor daporinad alone causes cell death and exacerbates the combination-induced cytotoxicity. Together, these findings indicate that DMG is highly dependent on adequate NAD^+ and that the synergistic effect of panobinostat and marizomib is driven, in large part, by their effect on cellular metabolism. Further studies will more definitively establish the mechanistic basis for the observed synergy.

The application of marizomib, a blood-brain barrier penetrant proteasome inhibitor, in CNS tumors has been proposed as a potential therapeutic strategy in glioblastoma (*19*, *20*, *23*, *39*). This strategy is further supported by the observation that marizomib has an effect on CNS metastases of multiple myeloma, providing evidence of brain penetrance (*40*). In DIPG, interim analysis of an ongoing clinical trial for panobinostat (NCT02717455) has demonstrated early evidence of clinical benefit (*9*). Given the role combination therapy has played in treating other cancers, our data support exploring a clinical trial of panobinostat together with marizomib in DMGs. Although the effect size of the combination-induced increase in overall survival in this study is admittedly modest (~20%), this therapeutic benefit represents a substantial step toward changing the prognosis of DMGs. Ultimately, the development of effective, multipronged clinical strategies targeting cell-intrinsic vulnerabilities together with microenvironmental dependencies and immunotherapeutic opportunities provides hope for overcoming this devastating disease.

MATERIALS AND METHODS

Study design

This study was designed to identify and validate combination therapeutic candidates for DMGs. High-throughput single-agent and combination drug screening was performed as described and as previously reported (*16*). In vitro and in vivo xenograft experiments were conducted for top combination candidates. Selection of compounds for combination testing was determined by considering individual agent efficacy, current clinical status, brain penetrance, and mechanistic interest/enrichment.

Randomization

Mice xenografted with luciferase-expressing tumors were randomized into treatment conditions after baseline imaging to normalize for initial bioluminescence signal. Mice xenografted with SU-DIPG-XIII-P* tumors were randomized into treatment groups before treatment initiation.

Blinding

Experimenters were blinded to conditions for histological image acquisition and analysis.

Replication

All in vitro validation experiments were performed at least in triplicate. Sample sizes for all in vivo xenograft experiments are reported in their respective figure legends. For single-agent bioluminescence experiments, a minimum group n of 3 was calculated to have 80% power to detect a twofold change in signal on two-tailed t test, with estimated variance as calculated from previous experiments. For analysis of variance (ANOVA) of combination-agent bioluminescence experiments, a minimum group n of 3 was calculated to have 80% power given four treatment groups with estimated variance as calculated from previous bioluminescence experiments. For survival analyses, a total cohort size of 13 animals was calculated to have 80% power to detect a 20% increase in overall survival.

Patient-derived tumor cell cultures

For all human tissue studies, informed consent was obtained and Institutional Review Board approval was granted at each participating institution. Primary DMG cell culture models (SU-DIPG-IV, SU-DIPG-VI, SU-DIPG-XIII, SU-DIPG-XVII, SU-DIPG-XXI, SU-DIPG-XXV, VU-DIPG-10, JHH-DIPG-I, and QCTB-R059) have been previously described (*8*, *10*, *29*, *30*). SU-pSCG-1 was cultured at time of autopsy as previously described (*41*). All cultures were maintained as neurospheres in tumor stem medium consisting of Neurobasal(-A) (Invitrogen), B27(-A) (Invitrogen), human basic fibroblast growth factor (bFGF) (20 ng/ml) (Shenandoah Biotechnology), human epidermal growth factor (EGF) (20 ng/ml) (Shenandoah), human platelet-derived growth factor (PDGF)–AB (20 ng/ml) (Shenandoah), and heparin (10 ng/ml). All cell culture models were validated by short tandem repeat (STR) DNA fingerprinting and routinely tested for mycoplasma. Information about age, sex, and clinical characteristics associated with each cell culture can be found in table S10.

In vivo xenograft models and bioluminescence analysis

All animal procedures were performed with approval from the Stanford University Administrative Panel on Laboratory Animal Care and adhered to the National Institutes of Health *Guide for the Care and Use of Laboratory Animals*. Both male and female animals were used equally.

Patient-derived pontine xenografts were generated as previously described (*8*, *10*, *29*, *30*). Briefly, a single-cell suspension was made from DIPG neurospheres, and cells were stereotactically injected into NOD-SCID-IL2 γ chain–deficient (NSG) cold-anesthetized mouse pups on postnatal day 2 (P2) or isoflurane-anesthetized mice on P35. SU-DIPG-VI-GFP luc xenografts were performed on P2 mouse pups through a 31-gauge burr hole (coordinates: 3.0 mm posterior to lambda suture and 3.0 mm deep) using 100,000 cells in 2-μl total volume. SU-DIPG-XIII-P* pontine xenografts were performed on P35 mice through a 26-gauge burr hole (coordinates: 0.8 mm right of midline, 1.0 mm posterior to lambda suture, 5.0 mm deep) using

300,000 cells in 3-μl total volume. Other injection sites in P35 mice included SU-pSCG-1 medulla xenografts (coordinates: 0.7 mm right of midline, 3.7 mm posterior to lambda suture, 4.5 mm deep) and QCTB-R059 thalamic xenografts (coordinates: 0.8 mm right of midline, 1.0 mm posterior to bregma suture, 3.5 mm deep).

In vivo bioluminescence imaging was performed weekly using an IVIS imaging system (Xenogen) under isoflurane anesthesia. Administration of panobinostat was performed with intraperitoneal injection 3 days per week (Monday, Wednesday, and Friday) at dose levels of 5 and 10 mg/kg. Panobinostat was dissolved in DMSO to 50 mg/ml and then diluted 1:50 in two parts polyethylene glycol (PEG) 300 (Hampton Research) and three parts 5% dextrose (Hospira). Administration of marizomib was performed with tail vein intravenous injection once per week (Monday) or twice per week (Monday and Thursday) at 150 μg/kg. Marizomib was dissolved in DMSO to 10 mg/ml and then diluted to 15 μg/ml in saline. Administration of BMS-754807 was performed with oral gavage 5 days per week (Monday, Tuesday, Wednesday, Thursday, and Friday) at 50 mg/kg. BMS-754807 was dissolved in four parts PEG 400 (Hampton Research) and one part water to 5 mg/ml. Administration of selumetinib was performed with oral gavage 5 days per week (Monday, Tuesday, Wednesday, Thursday, and Friday) at 100 mg/kg. Selumetinib was dissolved in 0.5% methylcellulose (Sigma-Aldrich) and 0.1% Tween 80 (Sigma-Aldrich) to 10 mg/ml. All controls were injected intraperitoneally, intravenously, or orally with an identical volume of the appropriate drug vehicle.

For IVIS analysis of in vivo DIPG tumor growth, animals were imaged at baseline. Animals were excluded if no tumors were present, and then animals were randomized to control and treatment groups such that each group had equivalent distribution of initial tumor sizes. For histological analysis of neurotoxicity after drug administration, mice were anesthetized with intraperitoneal injections of 2.5% Avertin (tribromoethanol; Sigma T48402) and transcardially perfused with 20 ml of 0.1 M phosphate-buffered saline.

Statistical analysis

Plots were drawn using GraphPad Prism and R software. Original numerical data are provided in table S11 in data file S1. Error bars represent means ± SEM. Statistical significance for in vitro and in vivo experiments was calculated using appropriate *t* test, ANOVA analyses, or Tukey's multiple comparisons test using GraphPad Prism, as indicated in the figure legends. Survival curves were analyzed using log-rank statistical testing in GraphPad Prism. Differentially expressed genes were estimated with DESeq2 Wald test with adjusted $P = 0.05$. An α level of 0.05 with two-sided testing was used unless otherwise specified. All data were normally distributed.

SUPPLEMENTARY MATERIALS

stm.sciencemag.org/cgi/content/full/11/519/eaaw0064/DC1
Materials and Methods
Fig. S1. MIPE library annotations, correlation analysis of MIPE 5.0 screens, and additional potency distributions.
Fig. S2. MoA similarities defined by clustering analyses of combination assessments.
Fig. S3. Combination assessments of drugs in active DIPG clinical evaluations.
Fig. S4. DIPG cell viability after treatment with candidate combinations.
Fig. S5. Flow cytometry analysis of BMS-754807– and selumetinib-treated DIPG cells.
Fig. S6. BMS-754807 and selumetinib in vivo alone or in combination with panobinostat and assessment of the effect of panobinostat and marizomib on brain viability.
Fig. S7. Efficacy of panobinostat alone and with marizomib on nonpontine DMG.
Fig. S8. Effect of extended treatment with panobinostat and marizomib on normal and malignant cell viability.
Fig. S9. Transcriptional responses to panobinostat and marizomib treatment in SU-DIPGXIII cells.
Fig. S10. GSEA of panobinostat and marizomib treatment in SU-DIPG-XIII cells.
Fig. S11. Transcriptional analysis of panobinostat and marizomib treatments in SU-DIPGVI and QCTB-R059 cells.
Fig. S12. Effects of panobinostat and marizomib treatment on ER stress and the UPR pathway in DIPG cells.
Fig. S13. Down-regulated transcriptional programs in SU-DIPG-VI and QCTB-R059 cells.
Fig. S14. Drug-induced metabolic rewiring and collapse in DIPG.
Fig. S15. Lack of rescue by the ROS mitigator *N*-acetylcysteine from proteasome inhibition and HDAC inhibitor–induced toxicity in DIPG.
Fig. S16. Effects of metabolic and NAD^+ perturbations on DIPG.
Data file S1 contains tables S1 to S11.
Table S1. Listing of all PubChem AIDs for all single-agent screening data.
Table S2. Complete listing of agents, MoAs, clinical phase, and CAS numbers for the MIPE 5.0 library.
Table S3. MoA distribution for all MIPE 5.0 library members.
Table S4. Complete listing of 371 potency-selected agents.
Table S5. Complete listing of agents in current or recently completed clinical trials for DIPG.
Table S6. Complete listing of agents with average *Z*-AUC < −2.0 and predicted CNS exposure (MPO score > 4.4).
Table S7. Complete listing of outcomes from the panobinostat "drug-versus-all" experiment in SU-DIPG-XXV.
Table S8. Complete listing of outcomes from the marizomib drug-versus-all experiment in SU-DIPG-XXV.
Table S9. Complete listing of outcomes from the 45-agent all-versus-all experiment in SU-DIPG-XXV.
Table S10. Characteristics of patient-derived high-grade glioma cell cultures.
Table S11. Original numerical data for experiments presented as composite graphs.
Reference (*42*)

View/request a protocol for this paper from *Bio-protocol*.

REFERENCES AND NOTES

1. T. B. Johung, M. Monje, Diffuse intrinsic pontine glioma: New pathophysiological insights and emerging therapeutic targets. *Curr. Neuropharmacol.* **15**, 88–97 (2017).
2. M. H. A. Jansen, D. G. van Vuurden, W. P. Vandertop, G. J. L. Kaspers, Diffuse intrinsic pontine gliomas: A systematic update on clinical trials and biology. *Cancer Treat. Rev.* **38**, 27–35 (2012).
3. T. Cooney, A. Lane, U. Bartels, E. Bouffet, S. Goldman, S. E. S. Leary, N. K. Foreman, R. J. Packer, A. Broniscer, J. E. Minturn, C.-S. Shih, M. Chintagumpala, T. Hassall, N. G. Gottardo, H. Dholaria, L. Hoffman, B. Chaney, J. Baugh, R. Doughman, J. L. Leach, B. V. Jones, M. Fouladi, K. E. Warren, M. Monje, Contemporary survival endpoints: An International Diffuse Intrinsic Pontine Glioma Registry study. *Neuro Oncol.* **19**, 1279–1280 (2017).
4. J. Schwartzentruber, A. Korshunov, X.-Y. Liu, D. T. W. Jones, E. Pfaff, K. Jacob, D. Sturm, A. M. Fontebasso, D.-A. Quang, M. Tönjes, V. Hovestadt, S. Albrecht, M. Kool, A. Nantel, C. Konermann, A. Lindroth, N. Jäger, T. Rausch, M. Ryzhova, J. O. Korbel, T. Hielscher, P. Hauser, M. Garami, A. Klekner, L. Bognar, M. Ebinger, M. U. Schuhmann, W. Scheurlen, A. Pekrun, M. C. Frühwald, W. Roggendorf, C. Kramm, M. Dürken, J. Atkinson, P. Lepage, A. Montpetit, M. Zakrzewska, K. Zakrzewski, P. P. Liberski, Z. Dong, P. Siegel, A. E. Kulozik, M. Zapatka, A. Guha, D. Malkin, J. Felsberg, G. Reifenberger, A. von Deimling, K. Ichimura, V. P. Collins, H. Witt, T. Milde, O. Witt, C. Zhang, P. Castelo-Branco, P. Lichter, D. Faury, U. Tabori, C. Plass, J. Majewski, S. M. Pfister, N. Jabado, Driver mutations in histone H3.3 and chromatin remodelling genes in paediatric glioblastoma. *Nature* **482**, 226–231 (2012).
5. D.-A. Khuong-Quang, P. Buczkowicz, P. Rakopoulos, X.-Y. Liu, A. M. Fontebasso, E. Bouffet, U. Bartels, S. Albrecht, J. Schwartzentruber, L. Letourneau, M. Bourgey, G. Bourque, A. Montpetit, G. Bourret, P. Lepage, A. Fleming, P. Lichter, M. Kool, A. von Deimling, D. Sturm, A. Korshunov, D. Faury, D. T. Jones, J. Majewski, S. M. Pfister, N. Jabado, C. Hawkins, K27M mutation in histone H3.3 defines clinically and biologically distinct subgroups of pediatric diffuse intrinsic pontine gliomas. *Acta Neuropathol.* **124**, 439–447 (2012).
6. D. N. Louis, A. Perry, G. Reifenberger, A. von Deimling, D. Figarella-Branger, W. K. Cavenee, H. Ohgaki, O. D. Wiestler, P. Kleihues, D. W. Ellison, The 2016 World Health Organization Classification of Tumors of the Central Nervous System: A summary. *Acta Neuropathol.* **131**, 803–820 (2016).
7. M. Gessi, G. H. Gielen, V. Dreschmann, A. Waha, T. Pietsch, High frequency of $H3F3A^{K27M}$ mutations characterizes pediatric and adult high-grade gliomas of the spinal cord. *Acta Neuropathol.* **130**, 435–437 (2015).
8. C. S. Grasso, Y. Tang, N. Truffaux, N. E. Berlow, L. Liu, M.-A. Debily, M. J. Quist, L. E. Davis, E. C. Huang, P. J. Woo, A. Ponnuswami, S. Chen, T. B. Johung, W. Sun, M. Kogiso, Y. Du,

L. Qi, Y. Huang, M. Hütt-Cabezas, K. E. Warren, L. Le Dret, P. S. Meltzer, H. Mao, M. Quezado, D. G. van Vuurden, J. Abraham, M. Fouladi, M. N. Svalina, N. Wang, C. Hawkins, J. Nazarian, M. M. Alonso, E. H. Raabe, E. Hulleman, P. T. Spellman, X.-N. Li, C. Keller, R. Pal, J. Grill, M. Monje, Functionally defined therapeutic targets in diffuse intrinsic pontine glioma. *Nat. Med.* **21**, 555–559 (2015).

9. T. Cooney, A. Onar-Thomas, J. Huang, R. R. Lulla, J. Fangusaro, K. Kramer, P. Baxter, M. Fouladi, I. J. Dunkel, K. E. Warren, M. Monje, DIPG-22. A phase 1 trial of the histone deacetylace inhibitor panobinostat in pediatric patients with recurrent or refractory diffuse intrinsic pontine glioma: A Pediatric Brain Tumor Consortion (PBTC) study. *Neuro Oncol.* **20**, i53 (2018).
10. S. Nagaraja, N. A. Vitanza, P. J. Woo, K. R. Taylor, F. Liu, L. Zhang, M. Li, W. Meng, A. Ponnuswami, W. Sun, J. Ma, E. Hulleman, T. Swigut, J. Wysocka, Y. Tang, M. Monje, Transcriptional dependencies in diffuse intrinsic pontine glioma. *Cancer Cell* **31**, 635–652. e6 (2017).
11. R. Hashizume, N. Andor, Y. Ihara, R. Lerner, H. Gan, X. Chen, D. Fang, X. Huang, M. W. Tom, V. Ngo, D. Solomon, S. Mueller, P. L. Paris, Z. Zhang, C. Petritsch, N. Gupta, T. A. Waldman, C. D. James, Pharmacologic inhibition of histone demethylation as a therapy for pediatric brainstem glioma. *Nat. Med.* **20**, 1394–1396 (2014).
12. A. Piunti, R. Hashizume, M. A. Morgan, E. T. Bartom, C. M. Horbinski, S. A. Marshall, E. J. Rendleman, Q. Ma, Y.-h. Takahashi, A. R. Woodfin, A. V. Misharin, N. A. Abshiru, R. R. Lulla, A. M. Saratsis, N. L. Kelleher, C. D. James, A. Shilatifard, Therapeutic targeting of polycomb and BET bromodomain proteins in diffuse intrinsic pontine gliomas. *Nat. Med.* **23**, 493–500 (2017).
13. F. Mohammad, S. Weissmann, B. Leblanc, D. P. Pandey, J. W. Hojfeldt, I. Comet, C. Zheng, J. V. Johansen, N. Rapin, B. T. Porse, A. Tvardovskiy, O. N. Jensen, N. G. Olaciregui, C. Lavarino, M. Suñol, C. de Torres, J. Mora, A. M. Carcaboso, K. Helin, EZH2 is a potential therapeutic target for H3K27M-mutant pediatric gliomas. *Nat. Med.* **23**, 483–492 (2017).
14. B. Al-Lazikani, U. Banerji, P. Workman, Combinatorial drug therapy for cancer in the post-genomic era. *Nat. Biotechnol.* **30**, 679–692 (2012).
15. L. H. Jones, M. E. Bunnage, Applications of chemogenomic library screening in drug discovery. *Nat. Rev. Drug Discov.* **16**, 285–296 (2017).
16. L. A. Mathews-Griner, R. Guha, P. Shinn, R. M. Young, J. M. Keller, D. Liu, I. S. Goldlust, A. Yasgar, C. McKnight, M. B. Boxer, D. Y. Duveau, J.-K. Jiang, S. Michael, T. Mierzwa, W. Huang, M. J. Walsh, B. T. Mott, P. Patel, W. Leister, D. J. Maloney, C. A. Leclair, G. Rai, A. Jadhav, B. D. Peyser, C. P. Austin, S. E. Martin, A. Simeonov, M. Ferrer, L. M. Staudt, C. J. Thomas, High-throughput combinatorial screening identifies drugs that cooperate with ibrutinib to kill activated B-cell–like diffuse large B-cell lymphoma cells. *Proc. Natl. Acad. Sci. U.S.A.* **111**, 2349–2354 (2014).
17. W. Ju, M. Zhang, K. M. Wilson, M. N. Petrus, R. N. Bamford, X. Zhang, R. Guha, M. Ferrer, C. J. Thomas, T. A. Waldmann, Augmented efficacy of brentuximab vedotin combined with ruxolitinib and/or Navitoclax in a murine model of human Hodgkin's lymphoma. *Proc. Natl. Acad. Sci. U.S.A.* **113**, 1624–1629 (2016).
18. T. T. Wager, X. Hou, P. R. Verhoest, A. Villalobos, Central nervous system multiparameter optimization desirability: Application in drug discovery. *ACS Chem. Neurosci.* **7**, 767–775 (2016).
19. R. H. Feling, G. O. Buchanan, T. J. Mincer, C. A. Kauffman, P. R. Jensen, W. Fenical, Salinosporamide A: A highly cytotoxic proteasome inhibitor from a novel microbial source, a marine bacterium of the new genus *salinospora*. *Angew. Chem. Int. Ed. Engl.* **42**, 355–357 (2003).
20. D. Chauhan, L. Catley, G. Li, K. Podar, T. Hideshima, M. Velankar, C. Mitsiades, N. Mitsiades, H. Yasui, A. Letai, H. Ovaa, C. Berkers, B. Nicholson, T.-H. Chao, S. T. C. Neuteboom, P. Richardson, M. A. Palladino, K. C. Anderson, A novel orally active proteasome inhibitor induces apoptosis in multiple myeloma cells with mechanisms distinct from Bortezomib. *Cancer Cell* **8**, 407–419 (2005).
21. T. Hideshima, J. E. Bradner, J. Wong, D. Chauhan, P. Richardson, S. L. Schreiber, K. C. Anderson, Small-molecule inhibition of proteasome and aggresome function induces synergistic antitumor activity in multiple myeloma. *Proc. Natl. Acad. Sci. U.S.A.* **102**, 8567–8572 (2005).
22. J. E. Amengual, P. Johannet, M. Lombardo, K. Zullo, D. Hoehn, G. Bhagat, L. Scotto, X. Jirau-Serrano, D. Radeski, J. Heinen, H. Jiang, S. Cremers, Y. Zhang, S. Jones, O. A. O'Connor, Dual targeting of protein degradation pathways with the selective HDAC6 inhibitor ACY-1215 and bortezomib is synergistic in lymphoma. *Clin. Cancer Res.* **21**, 4663–4675 (2015).
23. K. Di, G. K. Lloyd, V. Abraham, A. MacLaren, F. J. Burrows, A. Desjardins, M. Trikha, D. A. Bota, Marizomib activity as a single agent in malignant gliomas: Ability to cross the blood-brain barrier. *Neuro Oncol.* **18**, 840–848 (2016).
24. K. G. Halvorson, K. L. Barton, K. Schroeder, K. L. Misuraca, C. Hoeman, A. Chung, D. M. Crabtree, F. J. Cordero, R. Singh, I. Spasojevic, N. Berlow, R. Pal, O. J. Becher, M. M. Alonso, A high-throughput in vitro drug screen in a genetically engineered mouse model of diffuse intrinsic pontine glioma identifies BMS-754807 as a promising therapeutic agent. *PLOS ONE* **10**, e0118926 (2015).
25. T.-C. Chou, P. Talalay, Quantitative analysis of dose-effect relationships: The combined effects of multiple drugs or enzyme inhibitors. *Adv. Enzyme Regul.* **22**, 27–55 (1984).
26. A. Subramanian, P. Tamayo, V. K. Mootha, S. Mukherjee, B. L. Ebert, M. A. Gillette, A. Paulovich, S. L. Pomeroy, T. R. Golub, E. S. Lander, J. P. Mesirov, Gene set enrichment analysis: A knowledge-based approach for interpreting genome-wide expression profiles. *Proc. Natl. Acad. Sci. U.S.A.* **102**, 15545–15550 (2005).
27. P. Shannon, A. Markiel, O. Ozier, N. S. Baliga, J. T. Wang, D. Ramage, N. Amin, B. Schwikowski, T. Ideker, Cytoscape: A software environment for integrated models of biomolecular interaction networks. *Genome Res.* **13**, 2498–2504 (2003).
28. D. Merico, R. Isserlin, O. Stueker, A. Emili, G. D. Bader, Enrichment map: A network-based method for gene-set enrichment visualization and interpretation. *PLOS ONE* **5**, e13984 (2010).
29. H. S. Venkatesh, L. T. Tam, P. J. Woo, J. Lennon, S. Nagaraja, S. M. Gillespie, J. Ni, D. Y. Duveau, P. J. Morris, J. J. Zhao, C. J. Thomas, M. Monje, Targeting neuronal activity-regulated neuroligin-3 dependency in high-grade glioma. *Nature* **549**, 533–537 (2017).
30. C. W. Mount, R. G. Majzner, S. Sundaresh, E. P. Arnold, M. Kadapakkam, S. Haile, L. Labanieh, E. Hulleman, P. J. Woo, S. P. Rietberg, H. Vogel, M. Monje, C. L. Mackall, Potent antitumor efficacy of anti-GD2 CAR T cells in H3-K27M$^+$ diffuse midline gliomas. *Nat. Med.* **24**, 572–579 (2018).
31. C. S. Mitsiades, N. S. Mitsiades, C. J. McMullan, V. Poulaki, R. Shringarpure, T. Hideshima, M. Akiyama, D. Chauhan, N. Munshi, X. Gu, C. Bailey, M. Joseph, T. A. Libermann, V. M. Richon, P. A. Marks, K. C. Anderson, Transcriptional signature of histone deacetylase inhibition in multiple myeloma: Biological and clinical implications. *Proc. Natl. Acad. Sci. U.S.A.* **101**, 540–545 (2004).
32. S. Jagannath, M. A. Dimopoulos, S. Lonial, Combined proteasome and histone deacetylase inhibition: A promising synergy for patients with relapsed/refractory multiple myeloma. *Leuk. Res.* **34**, 1111–1118 (2010).
33. T. Hideshima, P. G. Richardson, K. C. Anderson, Mechanism of action of proteasome inhibitors and deacetylase inhibitors and the biological basis of synergy in multiple myeloma. *Mol. Cancer Ther.* **10**, 2034–2042 (2011).
34. D. R. Premkumar, E. P. Jane, N. R. Agostino, J. D. DiDomenico, I. F. Pollack, Bortezomib-induced sensitization of malignant human glioma cells to vorinostat-induced apoptosis depends on reactive oxygen species production, mitochondrial dysfunction, Noxa upregulation, Mcl-1 cleavage, and DNA damage. *Mol. Carcinog.* **52**, 118–133 (2011).
35. D. Buglio, V. Mamidipudi, N. M. Khaskhely, H. Brady, C. Heise, J. Besterman, R. E. Martell, K. MacBeth, A. Younes, The class-I HDAC inhibitor MGCD0103 induces apoptosis in Hodgkin lymphoma cell lines and synergizes with proteasome inhibitors by an HDAC6-independent mechanism. *Br. J. Haematol.* **151**, 387–396 (2010).
36. S. Kikuchi, R. Suzuki, H. Ohguchi, Y. Yoshida, D. Lu, F. Cottini, J. Jakubikova, G. Bianchi, T. Harada, G. Gorgun, Y.-T. Tai, P. G. Richardson, T. Hideshima, K. C. Anderson, Class IIa HDAC inhibition enhances ER stress-mediated cell death in multiple myeloma. *Leukemia* **29**, 1918–1927 (2015).
37. M. G. Vander Heiden, Targeting cancer metabolism: A therapeutic window opens. *Nat. Rev. Drug Discov.* **10**, 671–684 (2011).
38. M. G. Vander Heiden, R. J. DeBerardinis, Understanding the intersections between metabolism and cancer biology. *Cell* **168**, 657–669 (2017).
39. C. A. Manton, B. Johnson, M. Singh, C. P. Bailey, L. Bouchier-Hayes, J. Chandra, Induction of cell death by the novel proteasome inhibitor marizomib in glioblastoma in vitro and in vivo. *Sci. Rep.* **6**, 18953 (2016).
40. A. Badros, Z. Singh, B. Dhakal, Y. Kwok, A. MacLaren, P. Richardson, M. Trikha, P. Hari, Marizomib for central nervous system-multiple myeloma. *Br. J. Haematol.* **177**, 221–225 (2017).
41. G. L. Lin, M. Monje, A protocol for rapid post-mortem cell culture of Diffuse Intrinsic Pontine Glioma (DIPG). *J. Vis. Exp.* **121**, 10.3791/55360, (2017).
42. M. I. Love, W. Huber, S. Anders, Moderated estimation of fold change and dispersion for RNA-seq data with DESeq2. *Genome Biol.* **15**, 550 (2014).
43. J. Inglese, D. S. Auld, A. Jadhav, R. L. Johnson, A. Simeonov, A. Yasgar, W. Zheng, C. P. Austin, Quantitative high-throughput screening: A titration-based approach that efficiently identifies biological activities in large chemical libraries. *Proc. Natl. Acad. Sci. U.S.A.* **103**, 11473–11478 (2006).

Acknowledgments: We thank Celgene (formerly Triphase) for providing marizomib for animal studies, A. Moore and C. Jones for providing the QCTB-R059 culture and E. Hulleman for providing the VU-DIPG-10 culture. **Funding:** The study was supported by Alex's Lemonade Stand Foundation (to M.M.), Izzy's Infantry Foundation (to M.M.), McKenna Claire Foundation (to M.M.), Unravel Pediatric Cancer (to M.M.), Michael Mosier

Defeat DIPG Foundation (to M.M.), ChadTough Foundation (to M.M.), N8 Foundation (to M.M.), Kortney Rose Foundation (to M.M.), Cure Starts Now Foundation and the DIPG Collaborative (to M.M.), Sam Jeffers Foundation (to M.M.), Lyla Nsouli Foundation (to M.M.), Abbie's Army Foundation (to M.M.), Waxman Family Research Fund (to M.M.), Virginia and D.K. Ludwig Fund for Cancer Research (to M.M.), National Institute for Neurological Disorders and Stroke (R01NS092597 to M.M.) and NIH Director's Common Fund, (DP1NS111132 to M.M.), Maternal and Child Health Research Institute at Stanford (to M.M., A.C.G., and S.K.), the Anne T. and Robert M. Bass Endowed Faculty Scholarship in Pediatric Cancer and Blood Diseases (to M.M.), National Institute of Aging (RF1AG058047 to K.I.A.), DIPG All-In Initiative (to K.E.W.), and the NCATS and NCI intramural programs. B.Z.S. was supported as a St. Baldrick's Foundation Scholar. **Author contributions:** G.L.L., K.M.W., B.Z.S., P.J.W., S.K., E.Y.Q., X.Z., J.L., S.N., M.Q., S.M.G., C.K.-T., C.M., P.M., R.G., A.C.G., L.N., and N.A.V. performed the experiments. G.L.L., K.M.W., N.A.V., B.Z.S., M.C., P.J.W., S.K., E.Y.Q., X.Z., J.L., S.N., P.J.M., M.Q., D.Y.D., A.M.M., P.S., R.G., M.F., C.K.-T., S.M., C.M., P.M., Z.I., E.H.R., L.C., R.G., A.C.G., L.N., and K.I.A. analyzed the data. G.L.L., M.C., C.J.T., and M.M. wrote the paper. K.E.W., C.J.T., and M.M. conceived the project. C.J.T. and M.M. supervised all aspects of the work. **Competing interests:** The authors declare that they have no competing interests. **Data and materials availability:** All data associated with this study are present in the paper or the Supplementary Materials or through publicly accessible domains (RNA sequencing: GSE123278; PubChem AIDs are available in table S1). All patient-derived DIPG cell cultures named "SU" are available from M.M. under a material transfer agreement with Stanford University; the JHH-DIPG-1 culture is available from E.H.R.

Submitted 9 November 2018
Resubmitted 22 July 2019
Accepted 31 October 2019
Published 20 November 2019
10.1126/scitranslmed.aaw0064

Citation: G. L. Lin, K. M. Wilson, M. Ceribelli, B. Z. Stanton, P. J. Woo, S. Kreimer, E. Y. Qin, X. Zhang, J. Lennon, S. Nagaraja, P. J. Morris, M. Quezada, S. M. Gillespie, D. Y. Duveau, A. M. Michalowski, P. Shinn, R. Guha, M. Ferrer, C. Klumpp-Thomas, S. Michael, C. McKnight, P. Minhas, Z. Itkin, E. H. Raabe, L. Chen, R. Ghanem, A. C. Geraghty, L. Ni, K. I. Andreasson, N. A. Vitanza, K. E. Warren, C. J. Thomas, M. Monje, Therapeutic strategies for diffuse midline glioma from high-throughput combination drug screening. *Sci. Transl. Med.* **11**, eaaw0064 (2019).

Science Translational Medicine

Therapeutic strategies for diffuse midline glioma from high-throughput combination drug screening

Grant L. Lin, Kelli M. Wilson, Michele Ceribelli, Benjamin Z. Stanton, Pamelyn J. Woo, Sara Kreimer, Elizabeth Y. Qin, Xiaohu Zhang, James Lennon, Surya Nagaraja, Patrick J. Morris, Michael Quezada, Shawn M. Gillespie, Damien Y. Duveau, Aleksandra M. Michalowski, Paul Shinn, Rajarshi Guha, Marc Ferrer, Carleen Klumpp-Thomas, Sam Michael, Crystal McKnight, Paras Minhas, Zina Itkin, Eric H. Raabe, Lu Chen, Reem Ghanem, Anna C. Geraghty, Lijun Ni, Katrin I. Andreasson, Nicholas A. Vitanza, Katherine E. Warren, Craig J. Thomas and Michelle Monje

Sci Transl Med **11**, eaaw0064.
DOI: 10.1126/scitranslmed.aaw0064

A systematic attack against brain tumors

Diffuse midline gliomas are aggressive childhood brain tumors that are difficult to access surgically and therefore universally lethal. To search for potential therapeutic options for this devastating cancer, Lin *et al.* performed high-throughput screening on patient-derived glioma cells, followed by validation in cell cultures and mouse models of the disease. With this approach, the authors identified some potentially useful drug combinations, with the most promising one being that of the epigenetic targeting treatment panobinostat and the proteasome inhibitor marizomib. The authors also investigated the mechanism of the proposed therapeutic combination, linking its effectiveness to the induction of metabolic catastrophe in the tumor cells.

Science Translational Medicine (ISSN 1946-6242) is published by the American Association for the Advancement of Science, 1200 New York Avenue NW, Washington, DC 20005. The title *Science Translational Medicine* is a registered trademark of AAAS.